remote sensing

MDPI

Article

Vegetative Index Intercalibration Between PlanetScope and Sentinel-2 Through a SkySat Classification in the Context of "Riserva San Massimo" Rice Farm in Northern Italy

Christian Massimiliano Baldin * and Vittorio Marco Casella

Department of Civil Engineering and Architecture, University of Pavia, 27100 Pavia, Italy; vittorio.casella@unipv.it

* Correspondence: christianmassimiliano.baldin@unipv.it

Abstract: Rice farming in Italy accounts for about 50% of the EU's rice area and production. Precision agriculture has entered the scene to enhance sustainability, cut pollution, and ensure food security. Various studies have used remote sensing tools like satellites and drones for multispectral imaging. While Sentinel-2 is highly regarded for precision agriculture, it falls short for specific applications, like at the "Riserva San Massimo" (Gropello Cairoli, Lombardia, Northern Italy) rice farm, where irregularly shaped crops need higher resolution and frequent revisits to deal with cloud cover. A prior study that compared Sentinel-2 and the higher-resolution PlanetScope constellation for vegetative indices found a seasonal miscalibration in the Normalized Difference Vegetation Index (NDVI) and in the Normalized Difference Red Edge Index (NDRE). Dr. Agr. G.N. Rognoni, a seasoned agronomist working with this farm, stresses the importance of studying the radiometric intercalibration between the PlanetScope and Sentinel-2 vegetative indices to leverage the knowledge gained from Sentinel-2 for him to apply variable rate application (VRA). A high-resolution SkySat image, taken almost simultaneously with a pair of Sentinel-2 and PlanetScope images, offered a chance to examine if the irregular distribution of vegetation and barren land within rice fields might be a factor in the observed miscalibration. Using an unsupervised pixel-based image classification technique on SkySat imagery, it is feasible to split rice into two subclasses and intercalibrate them separately. The results indicated that combining histograms and agronomists' expertise could confirm SkySat classification. Moreover, the uneven spatial distribution of rice does not affect the seasonal miscalibration object of past studies, which can be adjusted using the methods described here, even with images taken four days apart: the first method emphasizes accuracy using linear regression, histogram shifting, and histogram matching; whereas the second method is faster and utilizes only histogram matching.

Keywords: PlanetScope; Sentinel-2; SkySat; remote sensing; NDVI; NDRE; classification; histogram; calibration; rice

check for updates

Citation: Baldin, C.M.; Casella, V.M. Vegetative Index Intercalibration Between PlanetScope and Sentinel-2 Through a SkySat Classification in the Context of "Riserva San Massimo" Rice Farm in Northern Italy. *Remote Sens.* **2024**, *16*, 3921. https://doi.org/10.3390/rs16213921

Academic Editors: Sebastien Clerc, Bahjat Alhammoud, Pierre Féménias, Jean Christopher Lambert and Steffen Dransfeld

Received: 28 August 2024
Revised: 9 October 2024
Accepted: 19 October 2024
Published: 22 October 2024

Copyright: © 2024 by the authors. Licensee MDPI, Basel, Switzerland. This article is an open access article distributed under the terms and conditions of the Creative Commons Attribution (CC BY) license (https://creativecommons.org/licenses/by/4.0/).

1. Introduction

1.1. Context of Rice Farming in Italy

In recent years, rice cultivation in Italy (which represents about 50% of EU rice area and production [1–7]) has faced additional challenges [8–10], including water scarcity during droughts [11], and rising fertilizer costs [12–15]. Russia's exit from European trade has intensified the issue [12], resulting in higher prices for nitrogen-based fertilizers, which affect the production chain and can also lead to pollution if overused. Consequently, farmers are exploring different strategies to maintain both the sustainability and productivity of their rice crops [14–17]. The adoption of precision farming techniques [14–21] may serve as a practical approach: it entails employing both remote and proximal sensing paired with data analysis to collect detailed insights on the agricultural crops and field conditions. Information collected through satellites, airplanes, drones, and tractors facilitates well-informed decisions on irrigation, weed control, fertilization, and harvesting, contributing

to improved resource utilization and enhanced agricultural yields. Rice plays a crucial role in Northern Italy's economy because of the extensive cultivation in the Po Valley [8–10,22]. This significant resource has been widely researched [10] and is the foundation for the doctorate upon which this study is based.

1.2. Precision Agriculture and VRA

In the realm of precision agriculture [15,17–21,23–33], variable rate application (VRA) [20,34,35] technology presents an innovative approach to the administration of chemical products. This technology allows for the exact application of chemicals based on prescription maps only when needed, reducing costs and enhancing food security [19]. Prescription maps must be created using remote and proximal sensing techniques, which allow for identifying and addressing specific needs in each crop area by generating vigor maps. These maps, which provide essential information for precision agriculture practices such as fertilizer application [18,21,31,33,36–49], herbicide usage [24,25,27,34,37,50–77], harvesting operations [32,37,40,41,69,78–87], and irrigation [9,26,34,45,62,65,88–91], can be generated through the study of vegetative indices derived from multispectral imagery. The bands [92–95] that make up these images facilitate the discernment of various areas within the field through numeric indices, each exhibiting varying degrees of crop health and vigor. Utilizing variable rate application (VRA) [20,34,35] offers substantial advantages: it enables farmers to decrease expenses and simultaneously enhance agricultural productivity. This approach also minimizes the risk of over-dosage, which can lead to nutrient leaching, water pollution, and greenhouse gas emissions. In addition to offering economic and ecological advantages, the application of variable rate application (VRA) and prescription maps in fertilization can enhance the quality of crops. Farmers can optimize plant growth, improve nutrient uptake, and reduce the risk of nutrient deficiencies by ensuring that crops receive the precise amount of product required. This may lead to healthier plants, better crop production, and improved product quality. Specialists in agronomy view variable rate application (VRA) [20,34,35] and prescription mapping as essential for making well-informed choices. By using these methods, agronomists can partner with farmers to create tailored strategies that consider the distinct characteristics of each crop and field. This cooperative method allows farmers to apply products knowledgeably, which often leads to enhanced yield, economic gain, and ecological endurance.

1.3. Remote Sensing and Vegetative Indices

Remote sensing, in the precision agriculture framework, is the process of obtaining information about an object or area from a distance. Vegetative indices [14,39,96–107] are mathematical transformations of remotely sensed data (bands) [93–95] that are used to estimate biophysical characteristics of vegetation, such as leaf area index, chlorophyll content, and biomass. The Normalized Difference Vegetation Index (NDVI) [82,108–113] and Normalized Difference Red Edge Index (NDRE) [17,35,49,88,112,114] are two of the most important remote sensing indices used in precision agriculture and in this paper [14,15,103,112,115]. They both provide information about the health and vigor of vegetation. The NDVI is calculated using the difference between the near-infrared (NIR) and red bands of the electromagnetic spectrum. NIR light is strongly reflected by healthy vegetation, while red light is absorbed. Therefore, NDVI values [115] are typically high for healthy vegetation and low for bare soil or unhealthy vegetation [96]. Typical ranges are $(-1, 0)$ for non-vegetated areas like buildings, soil, water, snow; (0, 0.2) for sparse vegetation or stressed vegetation; (0.2, 0.5) for moderate vegetation cover/low vegetation vigor; (0.6, 0.9) for dense vegetation cover/high vegetation vigor; and (0.8, 1) for very dense vegetation cover/very high vigor. The NDRE [103,112,114] is calculated using the difference between the red edge band and the red band. The red edge band is located at the boundary between the red and NIR bands, and it is sensitive to changes in chlorophyll content. Therefore, NDRE values are typically high for vegetation with high chlorophyll content (or healthier vegetation) and low for vegetation with low chlorophyll content (or

stressed vegetation) [112,116,117]. NDVI and NDRE are both involved in the process of fertilization and influence the selection of nitrogen uptake quantities through agronomic curves for fertilization [83,112,116,118,119]. Agronomists utilize tiles for crops, providing varying amounts of fertilization based on the values of these indices. NDRE is widely recognized as being more sensitive to changes in chlorophyll content, particularly in dense vegetation canopies, where NDVI may reach a point of saturation.

$$\text{NDVI} = \frac{\text{NIR} - \text{RED}}{\text{NIR} + \text{RED}} \tag{1}$$

$$\text{NDRE} = \frac{\text{NIR} - \text{RedEdge}}{\text{NIR} + \text{RedEdge}} \tag{2}$$

Additionally, this paper utilizes two other indices relevant to precision agriculture: MSAVI2 [120,121] and SR [97,102,103,107]. The MSAVI2 (Modified Soil Adjusted Vegetation Index 2) is designed to minimize the impact of soil background reflectance, especially in areas with low vegetation cover [116]. It is calculated using near-infrared (NIR) and red bands of the electromagnetic spectrum, similar to NDVI, but with a correction factor to reduce the influence of soil brightness [39]. The theoretical range of MSAVI2 is from -1 to 1. However, practical values for healthy vegetation typically fall between 0.2 and 0.8. SR is a simple ratio of near-infrared (NIR)-to-red (RED) reflectance. It is easy to calculate but can be affected by soil background and atmospheric conditions. SR is also prone to saturation in dense vegetation. The theoretical range of SR is from 0 to infinity. In practice, values for healthy vegetation typically range from 2 to 10 but can be much higher in dense canopies.

$$\text{MSAVI2} = \frac{1}{2} * (2 * \text{NIR} + 1 - \sqrt{(2 * \text{NIR} + 1)^2 - 8 * (\text{NIR} - \text{RED})}) \tag{3}$$

$$\text{SR} = \frac{\text{NIR}}{\text{RED}} \tag{4}$$

1.4. Relationship Between Agronomic Curves and Remote Sensing

In precision farming, an agronomic curve is an essential instrument that maps out the correlation between potential crop production and the quantity of a certain input applied, like fertilizer. In the context of the Normalized Difference Vegetation Index (NDVI) and Normalized Difference Red Edge (NDRE), agronomic curves can be particularly effective in determining the optimal amount of nitrogen fertilizer to apply to a crop [19,36,122–125]. The technique employs the use of NDVI or NDRE values as discriminating factors and calculates the quantity of chemicals required per tile based on these variables. Each point on the curve represents a specific level of input application (e.g., nitrogen fertilizer rate and the associated crop yield). The shape of the curve for fertilization often follows a parabolic trend, with an initial increase in yield as the input is applied, reaching a maximum yield at an optimal input level; beyond this point, further increases in input application may result in diminishing returns or even yield reductions due to excessive input application [46,47,85,86,126–128]. For this reason, the agronomic curve method has been unanimously identified as a valuable tool for fertilizer recommendations [18,20,46,83,86,112,126]. By identifying the point on the curve that corresponds to the highest yield, agronomists can determine the optimal amount of fertilizer to apply to achieve maximum crop productivity. This approach helps optimize fertilizer use efficiency, minimizing the risk of over-fertilization, which can lead to environmental problems and economic losses. By tracking changes in NDVI and NDRE values over time, agronomists can monitor crop growth and development, identifying areas of stress or potential yield limitations [16,17,23]. Agronomic curves can be used in conjunction with crop simulation models to predict yield potential based on various factors, including soil type, weather conditions, and management practices. Agronomic curves based on the NDVI and NDRE help agronomists improve crop yields by optimizing nitrogen fertilizer application, reduce fertilizer costs

by avoiding over-application, and minimize environmental impact by reducing nitrogen runoff [23,46,47,83,85,86,126–128], with enhanced food security [19].

1.5. Sentinel-2 as a Reference in Precision Agriculture

Sentinel-2 is considered a reference in precision agriculture [21,28,30,31,33,40–44,76,79,98,108,129–139] because of its high temporal and spatial resolution and its multispectral imaging capabilities [21,134]. Sentinel-2 offers a spatial resolution (10 m to 60 m) across 13 spectral bands [140–142], allowing for detailed crop monitoring and identification of variability within fields. With a revisit time of 5 days [143] (with both satellites A and B), it enables the timely detection of changes in crop health, growth stages, and stress factors. Sentinel-2's wide swath width (290 km) [144] allows for efficient monitoring of large agricultural areas, making it particularly useful for regional or national-scale analyses. The introduction of Sentinel-2 C could enable a reduction in revisit intervals [145].

The open-access policy of Sentinel-2 data democratizes precision agriculture technologies, making them accessible to farmers, researchers, and agricultural stakeholders worldwide. Sentinel-2 is a valuable asset for precision agriculture [15,17–21,23,31,33,40,79,133,134], providing high-quality data that can be leveraged to improve crop management practices, increase yields, and optimize resource utilization. With continued research and development, Sentinel-2 is poised to play an even more significant role in the future of sustainable agriculture.

1.6. The Need for Higher Spatial and Temporal Resolution

Sentinel-2 data are a valuable resource for precision agriculture [21,31,33,40,79,133,134], including land cover classification, vegetation monitoring, and disaster response. However, its 10 m spatial resolution and 5-day temporal frequency may be insufficient for applications like the "Riserva San Massimo" rice farm, which has small and irregularly shaped crops. The 10 m spatial resolution of Sentinel-2 data means that objects smaller than 10 m cannot be distinguished [146]. This issue can pose challenges for precision agriculture, according to Dr. Agr. G.N. Rognoni, an experienced agronomist who worked with the Ente Nazionale Risi [10,16,17,23,78] for many years. He emphasizes the importance of examining the radiometric intercalibration between PlanetScope and the Sentinel-2 vegetative indices NDVI and NDRE to utilize the insights obtained from Sentinel-2 in employing variable rate application (VRA) [20,35]. For instance, in Italy, where crop fields are often small and uneven, the detail provided by Sentinel-2 data might not be adequate for precise identification and monitoring of crops.

An issue known as the "edge effect" [147] could potentially be mitigated by implementing a buffer zone, although losing information [91] is not always beneficial. The 5-day temporal resolution of Sentinel-2 data means also that it is not possible to observe changes in land cover or vegetation that occur within a 5-day period [143]. This can be a problem for applications such as drought monitoring, where it is important to be able to track changes in vegetation health over time. Additionally, the 5-day temporal resolution may not be sufficient to capture rapid changes in vegetation, such as those caused by flooding or other natural disasters. In addition to these limitations, Sentinel-2 data can also be affected by cloud cover [14,15]. This means that it may not be possible to obtain cloud-free images of a particular area at the desired time. This can be a problem for applications that require consistent data availability, such as time-series analysis [14,15,131].

1.7. PlanetScope as a Valuable Resource

PlanetScope is a constellation of over 200 small satellites that provide daily high-resolution imagery of the Earth's surface [148]. These satellites are designed to work together to capture images of the entire planet every day, with a spatial resolution of 3 m and a temporal resolution of 1 day. This makes PlanetScope data ideal for applications that require high spatial and temporal resolution, such as precision agriculture [14,15,80,87,98,130,149,150], disaster response, and environmental monitoring. One of the key advantages of PlanetScope data is their

consistency over time and acquisitions, as demonstrated in previous papers [14,15]. Unlike traditional satellite imagery, which can be affected by cloud cover and other atmospheric conditions, PlanetScope images are always taken at the same time of day and under the same lighting conditions. This makes it possible to compare images from different dates and locations, and to track changes over time [150]. A challenge is the need to calibrate PlanetScope images to ensure that they are accurate and consistent [151]. Authors have realized this process in previous research, where a slight miscalibration has been found [14]. In various time frames, there is a necessity for the intercalibration of contemporary images [14,76,84,87,98,130,137,149,152–155] to enable the utilization of PlanetScope images when the Sentinel-2 reference is not accessible. This intercalibration process involves aligning the PlanetScope images with the Sentinel-2 images and correcting for any differences in the two datasets. This process is challenging [151], but it is essential to ensure that the PlanetScope images are accurate and consistent with the Sentinel-2 images.

1.8. Literature Review of Radiometric Intercalibration

Radiometric calibration ensures that the digital numbers (DNs) [156] in a satellite image can be accurately converted into physical units representing radiance or reflectance [122,157–160]. This is a crucial preprocessing step for quantitative analysis of satellite imagery, allowing for comparison across different sensors and time periods. Different sensors employ a mix of onboard and vicarious calibration methods [161] tailored to their specific characteristics and requirements [151,162–167]. PlanetScope [14,80,87,98,130,151–153,166,168–171] uses both onboard and vicarious calibration [161] techniques. Onboard, they utilize a solar calibration port and dark measurements. For vicarious calibration [161], they rely on PICS [165] (Pseudo-Invariant Calibration Sites) and cross-calibrate with Sentinel-2 data by comparing their data over the same area to adjust and match the radiometric responses of both sensors. Linear regression remains the most popular technique owing to its simplicity and speed in application and validation. It allows for straightforward assessment of how much it enhances the similarity between data being calibrated [138,172,173]. Histogram matching is an established method renowned for its effectiveness in numerous image processing applications thanks to its capability to align histogram distributions [132,174,175]. Histogram matching involves working with the cumulative distribution functions (CDFs) of both the source and reference images. The CDF of an image indicates the probability of a pixel value being less than or equal to a certain value. This process forms a transformation function by aligning the CDFs of the source and reference images, ensuring that the resulting image has a similar pixel value distribution to that of the reference image [158–160,174–177]. Histogram shifting is a technique used to adjust the distribution of pixel values within an image. It involves mapping the original pixel values to a new range, often to enhance contrast or match the histogram of one image to another. Histogram shifting has shown the ability to resolve issues related to atmospheric corrections [178]. It can also be applied for image normalization or preprocessing before further analysis [178–180].

1.9. Research Aims

PlanetScope offers a valuable solution for Earth observation and monitoring, but it can be challenging to calibrate contemporary PlanetScope images in various time frames. This becomes critical when the Sentinel-2 reference is not accessible, limiting the full utilization of PlanetScope data. To address this challenge, it is crucial to explore the role of uneven vegetation in miscalibration and find a suitable method for radiometric calibration of PlanetScope to Sentinel-2. The aims of the research are:

- Classify rice crops with subclasses of vegetation and barren land through SkySat images to perform separate radiometric intercalibration of PlanetScope/Sentinel-2.
- Conduct radiometric intercalibration when miscalibration is significant, using non-contemporary images taken within a 4-day interval, based on the current Sentinel-2 revisit time.

- Investigate both contemporary and conventional approaches, including linear regression and histogram matching, to identify the most effective method for aligning PlanetScope images with Sentinel-2 imagery.

2. Materials and Methods

2.1. Riserva San Massimo Rice Farm

"Riserva San Massimo" [181–186], located in the scenic countryside near Pavia, Italy, is a large agricultural establishment that was carefully chosen for this research (Figure 1). The work was performed in partnership with a renowned agronomic consulting team headed by Dr. Agr. P.A. Barbieri and Dr. Agr. G.L. Rognoni [14–17,23].

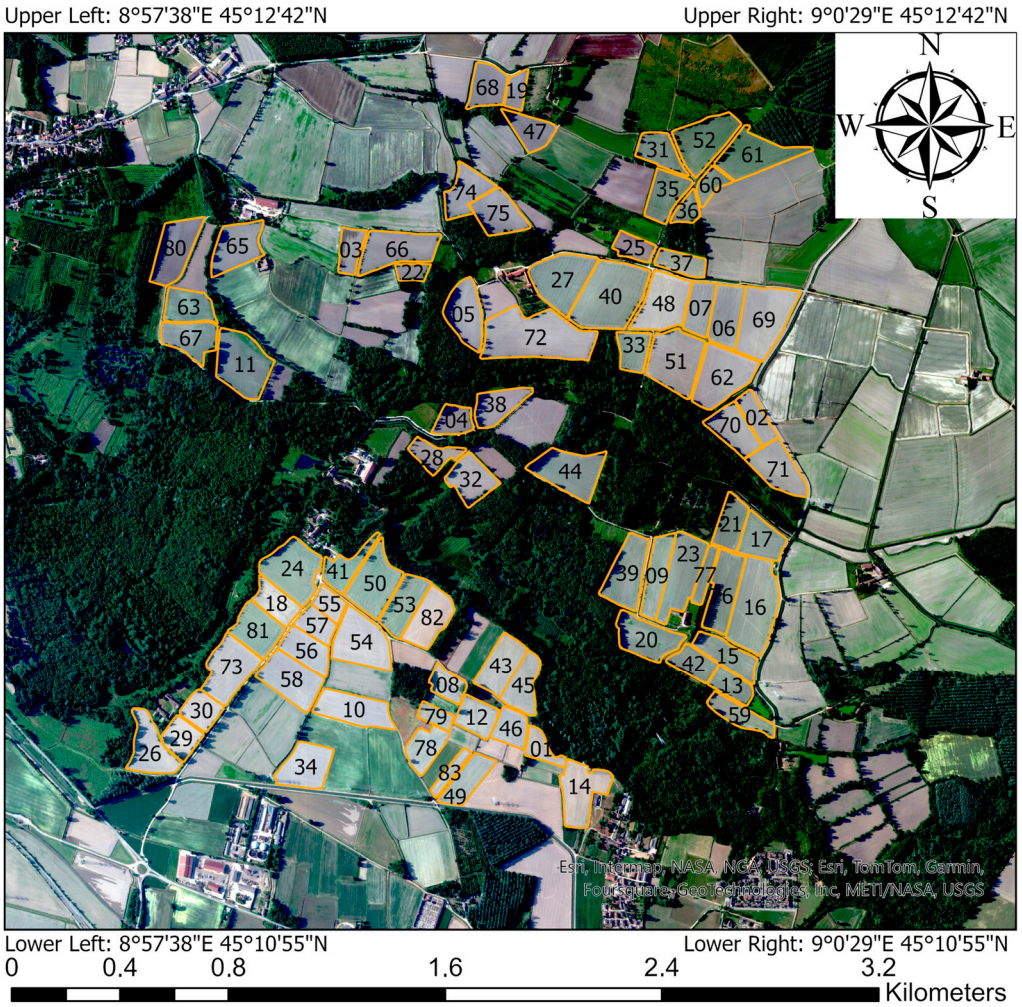

Figure 1. Riserva San Massimo rice farm crops over 3 June 2021. SkySat image—EPSG: 4326.

This distinctive reserve exemplifies a harmonious convergence of agricultural pursuits and wildlife preservation. Central to Riserva San Massimo's operations is the cultivation of rice (rice crops marked with a label in Figure 1) through the employment of organic farming practices. This sustainable approach prioritizes the utilization of natural methodologies and resources to uphold the ecological equilibrium of the farm's ecosystem. The rich, fertile soil and abundant water supply create optimal conditions for the cultivation of premium-quality rice, ensuring exceptional flavor and nutritional value. Within the confines of the reserve, a diverse array of wildlife species finds refuge and sustenance. Migratory birds flock to the wetlands, capitalizing on the bountiful nourishment and shelter provided by the farm's natural habitats. Foxes, hares, and badgers roam freely, while insects and amphibians assume critical roles in preserving the ecological balance. Riserva San Massimo

exemplifies the successful balance between agricultural practices and wildlife preservation. Through its unwavering commitment to organic farming practices and the preservation of natural habitats, the farm serves as a paradigm for sustainable land management and a sanctuary for countless species. The WGS84 UTM32N reference system (EPSG: 32632) was employed for the maps. In contrast, Figure 1 uses EPSG: 4326 due to its compatibility with standard web map servers. Figure 1 shows the crop numbers given by the agronomists for reference.

2.2. Sentinel-2

The Copernicus Sentinel-2 project operates with two polar-orbiting satellites [187–189], Sentinel-2A and Sentinel-2B, both in synchronized sun-synchronous orbits and staggered 180° apart [140,190]. This constellation design allows for a revisit time of 5 days for most areas of the world [143], which is essential for monitoring rapidly changing phenomena such as floods, wildfires, and vegetation growth. Copernicus [191] is a collaborative project between the European Space Agency (ESA) and the European Commission. It is the largest Earth observation program in the world, providing free and open access to data from a wide range of satellites and in situ sensors. Copernicus Sentinel-2 is one of the six Sentinel missions that are part of Copernicus. The Sentinel-2 mission provides high-resolution optical imagery in 13 spectral bands [142,192,193], including visible, near-infrared, and shortwave infrared wavelengths. The spatial resolution of the imagery varies from 10 m for the most important bands used in this research (red and NIR at 10; red edge at 20 m) to 60 m for the coastal aerosol band [146]. Sentinel-2 images are processed to produce two main product types: top of atmosphere (TOA) and bottom of atmosphere (BOA) [144]. TOA images represent the amount of light reflected by the Earth's surface, while BOA images represent the amount of light that would have been reflected if there were no atmosphere [144]. BOA images are typically used for applications that require accurate measurements of surface reflectance, such as land cover classification and vegetation monitoring. For this study, a level-2A bottom-of-atmosphere (BOA) Sentinel-2 image taken on 31 May 2021 was used, with a size of 53 MB after being cropped to the test site and including all bands resampled to 3 m.

Use of Sentinel-2 images is under license: Copernicus Sentinel satellite—Open Access compliant, CC BY-SA 3.0 IGO [194].

2.3. PlanetScope

The PlanetScope constellation [169,195] consists of more than 200 satellites, divided into three cohorts: PS2, PS2.SD, and PSB.SD [196–198]. The PSB.SD satellites, which were launched after August 2021, replaced the older satellites and provide an almost daily revisit time with 8 bands at 3 m resolution. These bands include green I, red edge, yellow, and coastal blue, in addition to the standard visible and near-infrared (VIS+NIR) bands. The red, red edge, and NIR bands of the PSB.SD satellites have wavelengths of 665 nm, 705 nm, and 865 nm, respectively, and a resolution of 3 m. PlanetScope offers two types of geometries for its satellite images [169]: orthorectified (chosen for this work) and non-orthorectified. Additional helpful details on PlanetScope imagery are available in the "Scene Level Normalization and Harmonization of Planet Dove Imagery" [170] document. It offers an in-depth look at the radiometric and geometric corrections applied to PlanetScope images and provides guidance for their application in scientific studies. The PlanetScope image for Riserva San Massimo, used in this study, was taken on 6 April 2021. The cropped image, focused on the test site, is 23 MB in size and features 8 bands with a 3 m resolution. The product comprises surface reflectance data presented as a rectified asset [198].

Use of PlanetScope images is under license: ©Planet Labs PBC, CC BY-NC-SA 2.0 [199].

2.4. Harmonization Between PlanetScope and Sentinel-2 Images

PlanetScope provides temporally and spatially consistent data that closely align with the spectral response of the Sentinel-2 satellite mission [170]. This harmonization is achieved by applying the "Sentinel-2" target sensor to all Doves, which are the individual satellites within the PlanetScope constellation. This ensures that all Dove sensors are consistent with each other and compatible with Sentinel-2 data. Specifically, only the red, green, blue, and near-infrared bands of the PlanetScope sensors are harmonized and normalized to match those of Sentinel-2 [151,170,171,200,201]. This harmonization process involves radiometric and geometric corrections to align the data from the different sensors, resulting in seamless integration and comparability [170]. However, it is important to note that the Sentinel-2 target sensor can be applied solely to the surface reflectance assets produced by PlanetScope. One exception to note is the SuperDove's (PSB.SD) red edge band, as the Normalized Difference Red Edge Index (NDRE) is calculated using a harmonized near-infrared (NIR) band and a non-harmonized red edge band. This disparity affects the NDRE, making it more difficult to calibrate in relation to the Normalized Difference Vegetation Index (NDVI) [14,15]. A characteristic of PlanetScope's NIR is its compatibility with Sentinel-2 band 8a, particularly the narrow near-infrared (NIR) band, and not with band 8 (the customary NIR extensively utilized with a finer resolution of 10 m and employed by agronomists and farmers for NDVI) [196,197]. This compatibility must be considered as the narrow NIR band has the potential to alleviate issues related to the presence of aerosols and its resolution is 20 m [129,167,187,202]: it generates an NDVI slightly different from the conventional, even when calculated using two compatible bands. "Scene Level Normalization and Harmonization of Planet Dove Imagery" [170] provide a comprehensive explanation of the processes involved in aligning PlanetScope's data with those of Sentinel-2, clarifying that this normalization is not always perfect and can lead to inconsistencies due to several factors: differences in sensor band responses between Dove and Sentinel-2 satellites, surface condition changes over time in a specific region, presence of large bodies of water in the image, and potential overcorrection during atmospheric correction. Additionally, since normalization is applied on a per-scene basis, visible differences may appear between adjacent scenes in a single strip [170].

2.5. SkySat

SkySat [151,203,204] is a constellation of 21 high-resolution Earth observation satellites operated by Planet Labs (like PlanetScope). They can capture sub-meter resolution imagery, making them ideal for a variety of applications such as monitoring, mapping, and disaster response. SkySat images are typically 50 cm per pixel resolution and can be collected, by request, multiple times per day over the same location. This allows for the monitoring of changes over time and the detection of events as they happen. The unique Skysat image actually available for "Riserva San Massimo" in archive is for 3 June 2021 (size 650 M), with red, green, blue, and NIR bands and a resolution of 0.5 m (with a real ground sample distance of 0.71). The SkySat image used in this paper is Analytic DN Ortho Scene, orthorectified, multispectral BGRN. The product has undergone processing to correct terrain-induced distortions and remove the perspective effect from ground features, realigning them with a vertical viewpoint geometry [151].

Use of SkySat images is under license: ©Planet Labs PBC, CC BY-NC-SA 2.0 [199].

2.6. Methods

2.6.1. Choosing Images

The dates of the PlanetScope and Sentinel-2 images were meticulously selected to align as closely as possible with the unique SkySat very high resolution and cloud-free acquisition [14,15]. This strategic choice ensured that the resulting analysis and insights were based on the most current and optimal data available. The independent SkySat classification allowed for the intercalibration of PlanetScope and Sentinel-2, facilitating an in-depth analysis. The closely matched acquisition dates, being within the Sentinel-2 revisit

period, reduced temporal changes and enabled a comparison of vegetation and barren land behavior between PlanetScope and Sentinel-2. Previous studies [14,15] confirmed that the highest RMSE occurred during this period, making the selection and the opportunity of this date critically important.

2.6.2. Choosing Bands for PlanetScope and Sentinel-2

Following consideration of the harmonization between PlanetScope and Sentinel-2, the Normalized Difference Vegetation Index (NDVI) and the Normalized Difference Red Edge Index (NDRE) were calculated, compared, and calibrated through these bands:

$$\mathrm{NDVI}_{\mathrm{Sentinel}-2} = \frac{\text{Band 8} - \text{Band 4}}{\text{Band 8} + \text{Band 4}} \quad (5)$$

$$\mathrm{NDVI}_{\mathrm{Planetscope}} = \frac{\text{Band 8} - \text{Band 6}}{\text{Band 8} + \text{Band 6}} \quad (6)$$

$$\mathrm{NDRE}_{\mathrm{Sentinel}-2} = \frac{\text{Band 8} - \text{Band 5}}{\text{Band 8} + \text{Band 5}} \quad (7)$$

$$\mathrm{NDRE}_{\mathrm{Planetscope}} = \frac{\text{Band 8} - \text{Band 7}}{\text{Band 8} + \text{Band 7}} \quad (8)$$

2.6.3. SkySat Image Elaboration to Find Uneven Vegetation

The ArcGIS Pro combine tool [205–207], used on the SkySat image, is a geoprocessing tool that combines multiple rasters into a single raster dataset. It works by assigning a unique integer value to each unique combination of input values, creating a new categorical raster. When using a multiband raster as input raster, all the bands of the raster are used. It does not perform any spatial analysis or processing on the input rasters, so it is fundamental to create a specific selection of bands in relationship to the phenomena which need to be studied. This study utilized vegetation indices, specifically NDVI, MSAVI2 and SR [102–107,116,206,207], for the empirical differentiation of rice crops in the two subclasses vegetation and barren land. This process needs to be seen as an unsupervised classification, because at the end of the process it is necessary to label founded classes. This technique is useful to understand data without relying on predefined labels or categories. Instead, the algorithm automatically identifies patterns and structures within the data, enabling the user to uncover hidden insights and relationships after the classification. In an unsupervised classification process [206,207], the dataset does not contain class labels: the algorithm analyzes the data, identifying similarities and differences among the data points. It then groups similar data points together, forming clusters or classes. These classes are created based solely on the inherent characteristics of the data, rather than being imposed by a human annotator. One of the key advantages of unsupervised classification is its ability to uncover patterns and structures that might not be immediately apparent to the human eye before the classification. By allowing the algorithm to identify these patterns without bias, it is possible to gain valuable insights into the underlying relationships within the data. This can be particularly useful in domains where the data are complex, making it challenging for humans to manually identify meaningful patterns. Furthermore, unsupervised classification can help us identify outliers and anomalies within the data [208]. These outliers can represent rare or unique cases that might be of interest for further investigation. By isolating these outliers, it is possible to gain a better understanding of the overall distribution of the data and identify potential areas for further research or analysis. Once the categorical raster with the classification was generated, it was imported into the MathWorks MATLAB software (R2023b) for further processing. This step aimed to produce two more masks within the full crop mask: one for vegetation and another for barren land. The MATLAB environment provided a range of tools and functions to manipulate and analyze the raster data. The imported categorical raster, containing the classification information, served as the basis for creating the vegetation and barren land masks. To create the vegetation mask,

a threshold was applied to the raster values. Pixels with values corresponding to vegetation classes were assigned a value of 1, while all other pixels were assigned a value of 0. This resulted in a binary mask [209], where 1 represented vegetation areas and 0 represented non-vegetation areas. Similarly, to create the barren land mask, a different threshold was applied to the raster values. Pixels with values corresponding to barren land classes were assigned a value of 1, while all other pixels were assigned a value of 0. This process resulted in another binary mask, where 1 represented barren land areas and 0 represented non-barren land areas. The utilization of MATLAB's capabilities facilitated the efficient and accurate creation of the vegetation and barren land masks. The resulting masks provided valuable information which was integrated with further histogram analysis in MATLAB.

2.6.4. Resampling

Resampling [210,211] images through ESRI ArcGIS Pro 3.3 [212] was a crucial step in processing images of various resolutions, enabling integration and analysis. The resolution employed during processing was set at 3 m, aligning with the resolution of PlanetScope. To achieve this, Sentinel-2 imagery, initially captured at 10 m (for NDVI) and 20 m (for NDRE), underwent oversampling to match the 3 m resolution. Moreover, the SkySat-classified raster for rice crops, including vegetation and barren land subclasses, was resampled to 3 m. The nearest neighbor algorithm [213] was employed for resampling, ensuring that the pixel values of the resampled images closely resembled the original images. By utilizing this technique, the integrity and accuracy of the image data were maintained while aligning the resolutions of different sources, allowing for effective image processing and analysis. Overall, the resampling process played a vital role in harmonizing image resolutions, facilitating the integration of multi-source imagery, and enabling comprehensive image processing workflows. This approach allowed for the extraction of meaningful insights and the generation of valuable information products from diverse image datasets.

2.6.5. Linear Regression (LR)

Linear regression [172] is a statistical technique that models the connection between a dependent variable, which requires prediction, and one or more explanatory variables that act as predictors. It assumes a linear relationship, meaning the dependent variable changes proportionally with changes in the independent variables. Linear regression was performed through "fitlm" [173], which is considered the most versatile function for fitting linear models due to its flexibility in model specification, its ability to handle categorical predictors, and its comprehensive statistical output: it is essential to utilize two matrices, one containing the predictor variables and the other containing the variable that requires prediction. In this study, the "fitlm" [173] function was applied to the NDVI and NDRE indices. Given the necessity of calibrating PlanetScope responses to those of Sentinel-2, it is crucial to establish a linear equation that, when provided with PlanetScope indices as input, can output values similar to those of Sentinel-2.

An example of linear regression [214] as applied in this paper is

$$Y = \beta_0 + \beta_1 * X + \varepsilon \quad (9)$$

where:

- Y is the dependent variable, representing the vectorialized matrix of PlanetScope pixel values;
- X is the independent variable, representing the vectorialized matrix of Sentinel-2 pixel values;
- β_0 is the intercept of the regression line;
- β_1 is the slope of the regression line;
- ε is the error term, representing the variability not explained by the model.

2.6.6. Histogram Shifting (HS)

Histogram shifting [177,215,216] is a technique in image processing that adjusts the pixel intensity distribution of an image according to a specified value. It involves manipulating the histogram of an image, which is a graphical representation of the frequency of occurrence of different intensity values. By shifting the histogram, it is possible to adjust the brightness, contrast, and overall appearance of the image. In the context of this study, histogram shifting is applied to equate the mean pixel intensity between a PlanetScope image and a Sentinel-2 image. This technique assists in aligning their average intensity values, thus facilitating the process of comparing and recognizing both the similarities and differences in the images; it further enhances the analysis of histogram comparisons. This method is utilized as a part of the intercalibration process in this work. In MATLAB, NDVI and NDRE are shown as matrices of pixel values at given positions. In this study, mean shifting is employed by transforming pixel values into vectors (v1 and v2). A histogram is then computed over these vectors: the analysis reveals that the mean value of PlanetScope exceeds that of Sentinel-2 for both NDVI and NDRE. Consequently, if v1 represents the reference (Sentinel-2) and v2 denotes the input (PlanetScope), histogram shifting follows the formula

$$\mathrm{v2}_{\mathrm{shifted}} = \mathrm{v2} - \mathrm{mean}(\mathrm{v2} - \mathrm{v1}) \tag{10}$$

The approach used in this paper to assess its effectiveness involves computing the histogram of the shifted PlanetScope vector and of the Sentinel-2 (reference).

2.6.7. Histogram Matching (HM)

Histogram matching [132,174–176] is a process whereby the intensity distribution (histogram) of an image is modified to correspond to the histogram of a reference image. The first step is histogram calculation: the histograms of both the input image and the reference image are computed, showing the frequency of occurrence of different pixel intensities for each image. The CDFs (cumulative distribution functions) [217] of both histograms are calculated. A CDF represents the probability that a pixel value is less than or equal to a specific intensity level. A mapping function (transformation mapping) is determined that links the CDF values of the input image to those of the reference image. This mapping is designed to equalize the probabilities of corresponding intensity levels between the two images. Each pixel in the input image is then transformed to a new intensity level based on the established mapping function (intensity transformation). The result is an image with an intensity distribution closer to that of the reference image. This technique is relevant for this work as an intercalibration step because satellite sensors can exhibit variations in their radiometric response. Histogram matching helps calibrate these images to a common reference, ensuring consistent measurements across datasets. The histogram matching used in this paper ensures that the NDVI and NDRE indices calculated from different images are comparable, even if the original images were captured under different conditions or by different sensors. This is crucial for monitoring trends over time or comparing indices. MATLAB's "imhistmatch" function simplifies the implementation of histogram matching. It processes both the input and reference images, delivering the transformed input image with the desired intensity distribution from the reference. The number of bins, after numerous attempts, was set to 6000. In this study, the intensity level matched corresponds to the NDVI or NDRE index and is detailed as a single band for each sensor, after index computation. The quality of the match depends on the similarity between the histograms of the input and reference images; substantial differences can result in unnatural outputs. In the case of multi-channel images (RGB), contrasting with this scenario, handling the intensity distributions does not preserve the color relationships: to preserve the original colors, it is advisable to apply histogram matching to each single channel independently or convert the image to a luminance space beforehand.

A brief mathematical analysis [157–160] of the concepts discussed can be performed using the following terms:

- I is the input image (PlanetScope);
- R is the reference image (Sentinel-2);
- h_I is the histogram of the input image (PlanetScope);
- h_R is the histogram of the reference image (Sentinel-2);
- k is the intensity level;
- I' is the input image (PlanetScope) matched through the reference (Sentinel-2);
- p is the pixel in input image (PlanetScope);
- p' is the pixel in the input image matched to the reference image;
- L is the total number of intensity levels;
- i is the intensity level in the PlanetScope image;
- j is the intensity level in the Sentinel-2 image.

First step: compute the histograms for both images.

Second step: compute the cumulative distribution functions (CDFs) for both images. The CDF is the cumulative sum of the histogram values:

$$CDF_h(k) = \sum_{i=0}^{k} h(i) \quad (11)$$

Third step: normalize the CDFs, dividing each CDF value by the maximum CDF value (which is the CDF value at $L - 1$). This normalizes the CDFs to a range of 0 to 1.

$$CDF_{h_{norm}}(k) = \frac{CDF_h(k)}{CDF_h(L-1)} \quad (12)$$

Fourth step: Create the mapping function M that maps the intensity levels of the PlanetScope image to the intensity levels of the Sentinel-2 image. For each intensity level i in the PlanetScope image, find the minimum intensity level j in the Sentinel-2 image where the normalized CDF of the PlanetScope image is less than or equal to the normalized CDF of the Sentinel-2 image. The mapping function is defined as

$$M(i) = \min\{j | CDF_{h_I}(i) \leq CDF_{h_R}(j)\} \quad (13)$$

Fifth step: Apply the mapping function to each pixel in the PlanetScope image to obtain the calibrated image I'. For each pixel p in the PlanetScope image, the corresponding pixel p′ in the calibrated image is given by

$$I'(p) = M(I(p)) \quad (14)$$

2.6.8. Intercalibration Statistics Through RMSE and MAE

The root-mean-square Error (RMSE) and mean absolute error (MAE) are two commonly used metrics for evaluating the performance of image processing algorithms [218]. Both RMSE and MAE measure the difference between the corresponding pixels of two images, but they do so in different ways. RMSE is the square root of the mean of the squared differences between the corresponding pixels of two images. This means that RMSE gives more weight to larger errors, which can be useful for identifying areas of an image where there are significant differences between the two images being compared. MAE is the mean of the absolute differences between the corresponding pixels of two images. This means that MAE gives equal weight to all errors, regardless of their size. This can be useful for identifying areas of an image where there are many small differences between the two images being compared. In general, RMSE is a more commonly used metric than MAE, as it is more sensitive to large errors. However, MAE can be useful in some cases, such as when the errors are expected to be small. RMSE and MAE are useful to understand some effects: RMSE is a measure of the overall magnitude of the error between two images and MAE is a measure of the average magnitude of the error between two images. RMSE is more sensitive to large errors than MAE. MAE is more sensitive to small errors than RMSE. RMSE is typically used to evaluate the performance of image processing algorithms

that are designed to reduce the overall magnitude of the error between two images. MAE is typically used to evaluate the performance of image processing algorithms that are designed to reduce the average magnitude of the error between two images.

$$\mathrm{RMSE}_{\mathrm{NDVI}} = \sqrt{\frac{1}{n}\sum_{i,j}(\mathrm{NDVI}_2(i,j) - \mathrm{NDVI}_1(i,j))^2)} \quad (15)$$

$$\mathrm{RMSE}_{\mathrm{NDRE}} = \sqrt{\frac{1}{n}\sum_{i,j}(\mathrm{NDRE}_2(i,j) - \mathrm{NDRE}_1(i,j))^2)} \quad (16)$$

$$\mathrm{MAE}_{\mathrm{NDVI}} = \frac{\sum_{i,j}|\mathrm{NDVI}_2(i,j) - \mathrm{NDVI}_1(i,j)|}{n} \quad (17)$$

$$\mathrm{MAE}_{\mathrm{NDRE}} = \frac{\sum_{i,j}|\mathrm{NDRE}_2(i,j) - \mathrm{NDRE}_1(i,j)|}{n} \quad (18)$$

2.7. Process Flowchart

Figure 2 embodies the process flowchart with different colors for each source.

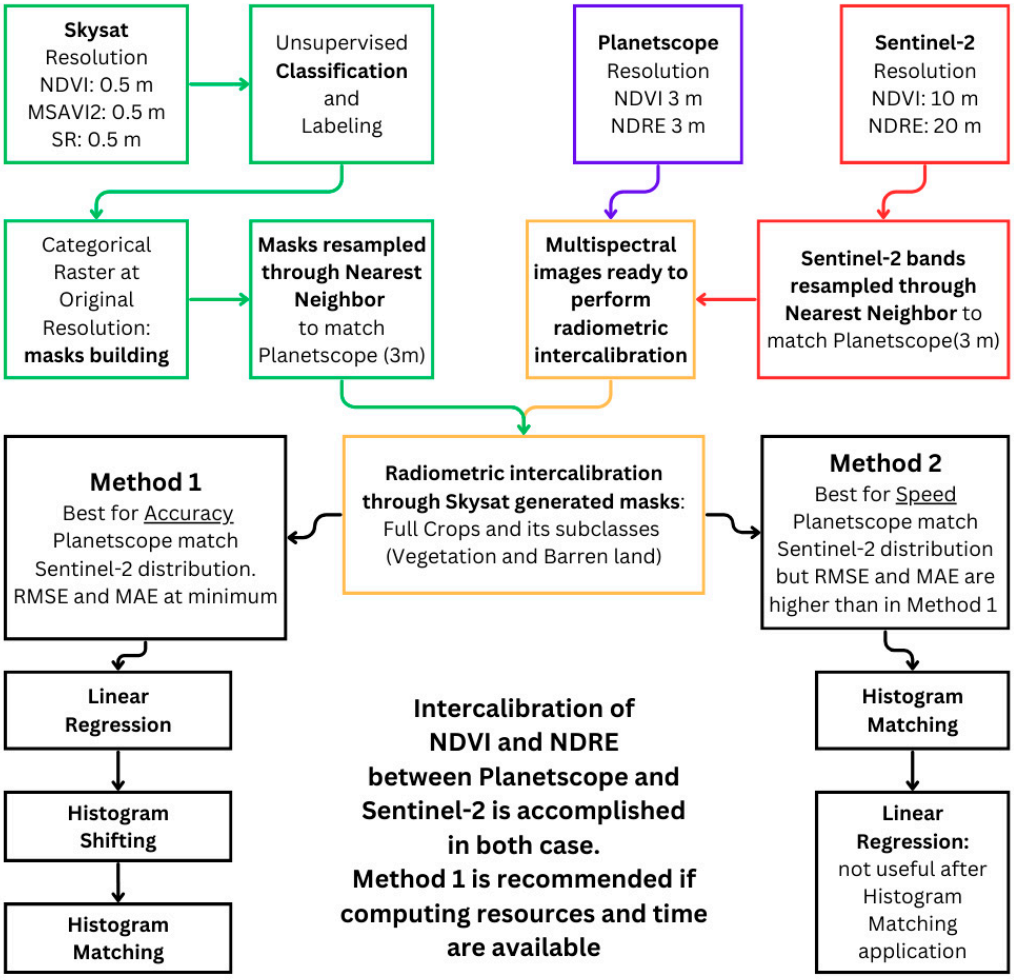

Figure 2. Process flowchart.

The initial phase, formally designated as the green line, exemplifies the unsupervised pixel-based classification methodology employed for the very high resolution SkySat image. This process utilizes the indices NDVI, MSAVI2, and SR. The outcome of this phase is the generation of masks, which are subsequently resampled and forwarded to the yellow radiometric intercalibration module. This module receives a dataset from the other yellow box,

which consists of multispectral images in need of calibration; this dataset originates from the PlanetScope image provided by the producer (blue line) and from Sentinel-2, with the image resampled to align with the PlanetScope resolution. The radiometric intercalibration block employs masks derived from the SkySat classification (represented by the green line) and from the multispectral imagery of PlanetScope and Sentinel-2 (indicated by the yellow line). Methodologies are indicated by black lines. Method 1, which was evaluated for its accuracy, encompasses linear regression, histogram shifting, and histogram matching. Method 2, which was assessed for its speed, includes histogram matching and linear regression (ultimately deemed unnecessary). Method 1 is recommended when computational resources and time are available. Both methods produce satisfactory outcomes in terms of intercalibration and the capacity to employ indices.

3. Results

3.1. SkySat Classification

Figure 3 presents the SkySat classification and employs EPSG: 4326 because of its compatibility with standard web map servers, allowing for quick allocation; the crop numbers are used by the agronomists for reference.

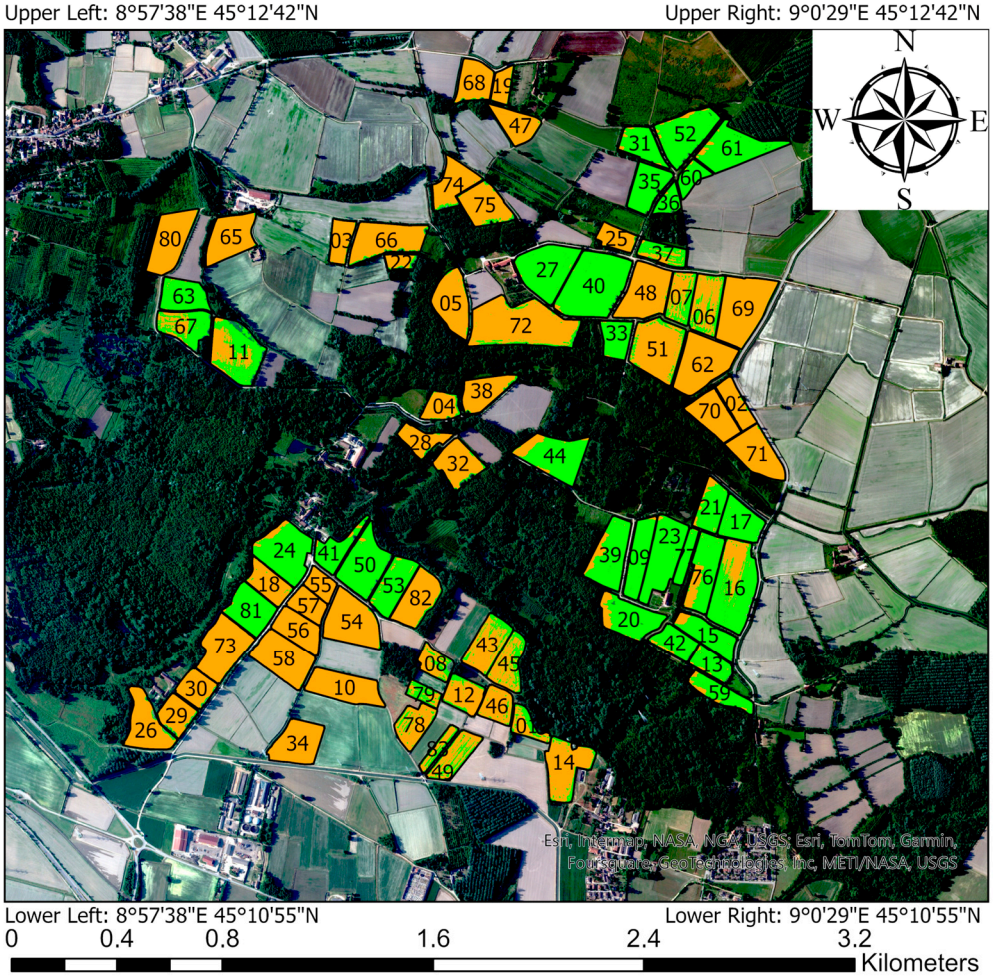

Figure 3. SkySat unsupervised classification with vegetation in green and barren land in brown.

SkySat's unsupervised pixel-based classification encompasses ninety-seven percent of the aggregate crop pixels, leaving merely three percent unidentified by the classification procedure (visual labeling was accomplished through the extremely high resolution provided). All the considered fields are planted with rice. The classification was conducted on the original resolution of the SkySat image, and then, it was resampled to a three-meter

resolution (PlanetScope resolution). The classification was used to calibrate rice crops, both combined and separately, with the two subclasses of growing vegetation and barren land. Figure 4 shows a zoom on crops numbered 27, 40, and 72, produced in MATLAB for intercalibration; binary masks are represented with white = true (1) and false = black (0). The edge effect phenomenon manifests itself prominently within the masking process, which is induced by the boundaries of the crop. This effect is a consequence of the existence of hybrid pixels that incorporate regions both outside and inside the crop boundary.

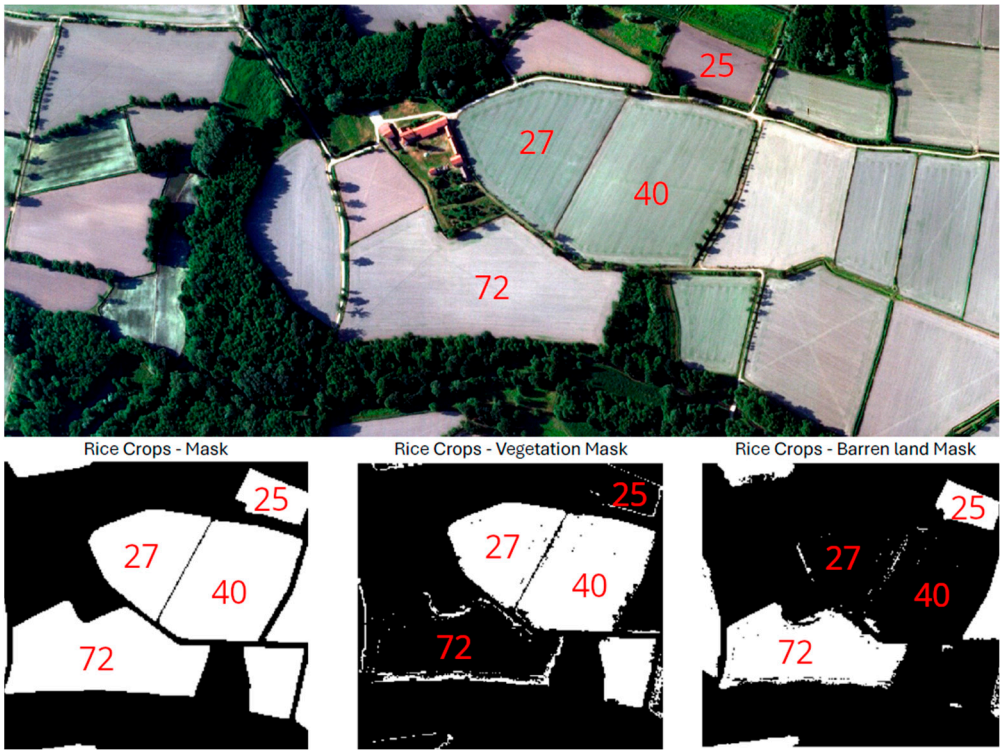

Figure 4. SkySat image compared with the masks produced in MATLAB.

3.2. Intercalibration PlanetScope/Sentinel-2

Within the context of the PlanetScope/Sentinel-2 intercalibration, two methodologies were identified as beneficial, as seen in the flow chart (Figure 2). Method 1 prioritizes accuracy, while method 2 prioritizes speed. In both intercalibration methodologies, the uneven presence of rice has a minimal and negligible influence on miscalibration. This can be observed through the RMSE and the MAE, which indicate that the difference for vegetation is slightly higher but still negligible. The intercalibration process is effective for both the NDVI and NDRE indices. It is important to note that although the red edge band of PlanetScope is not harmonized by its manufacturer, the methodologies remain successful.

3.3. Method 1

Figures 5 and 6 illustrate method 1 for NDVI and NDRE, respectively, showing similar histogram behaviors. PlanetScope indices have higher values, and after applying linear regression, the value distributions remain the same but shifted. RMSE and MAE significantly decrease post-regression, yet intercalibration does not resolve the differences fully. Histogram shifting reduces RMSE and MAE by aligning the PlanetScope histogram with Sentinel-2.

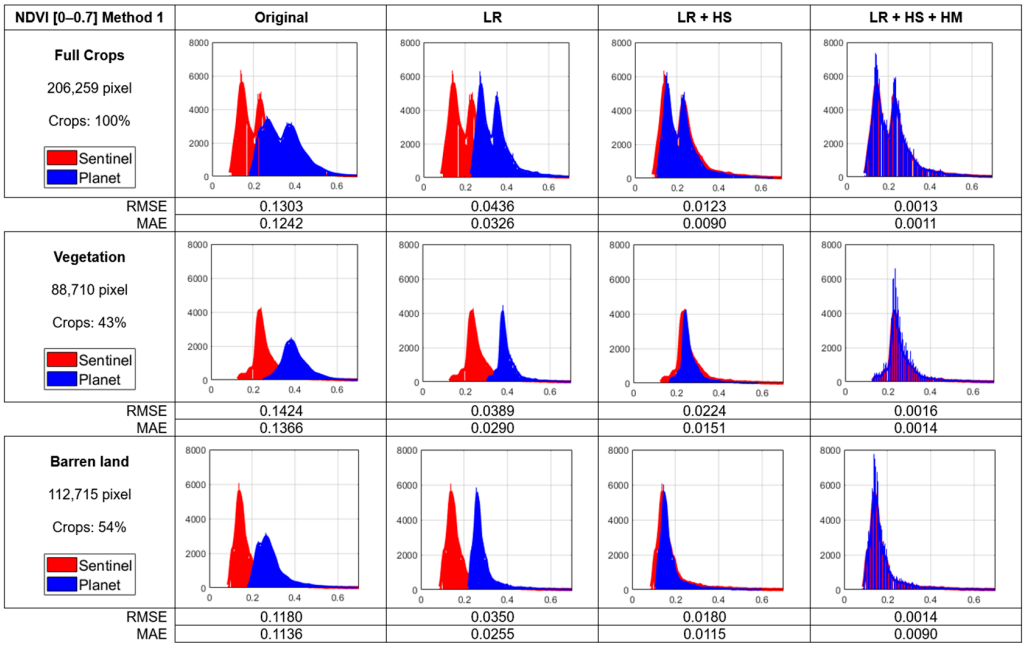

Figure 5. Method 1 for NDVI.

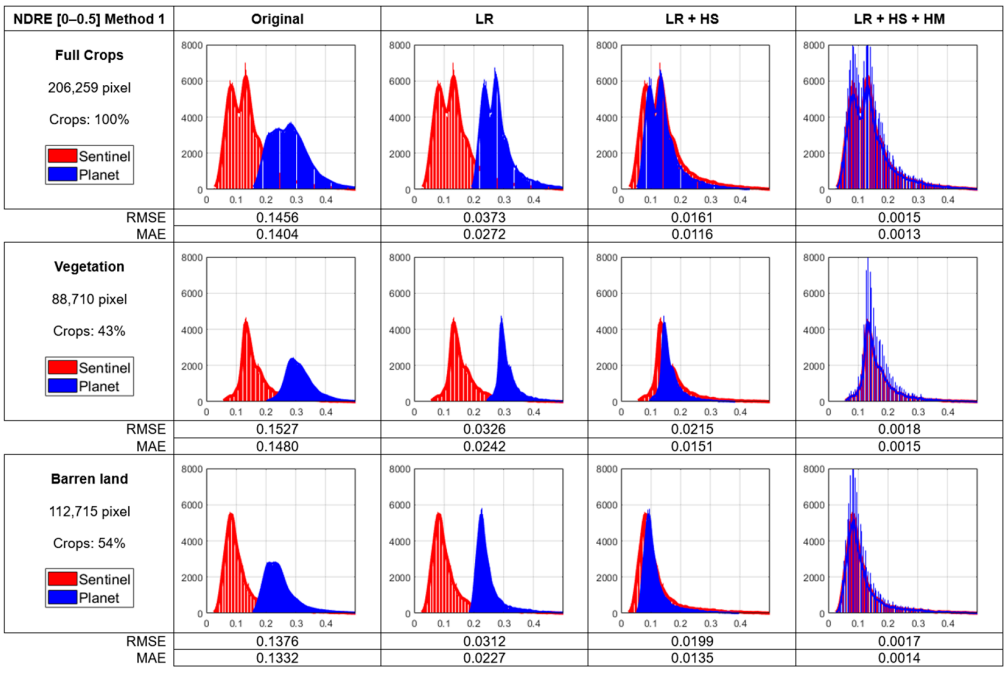

Figure 6. Method 1 for NDRE.

The final histogram matching step ensures nearly identical value distributions. The linear regression statistics can be found in Appendix A.

3.4. Method 2

Figures 7 and 8 demonstrate method 2 for NDVI and NDRE, respectively, also indicating similar initial histogram behaviors. PlanetScope indices exhibit higher values and following histogram matching the value distributions become superimposable even though RMSE and MAE are not as low as in the previous scenario. The key difference is that linear regression, which scales values uniformly, is not applied. After histogram matching, applying linear regression does not alter the outcome, making it unnecessary here. Therefore, method 2 relies solely on histogram matching for intercalibration.

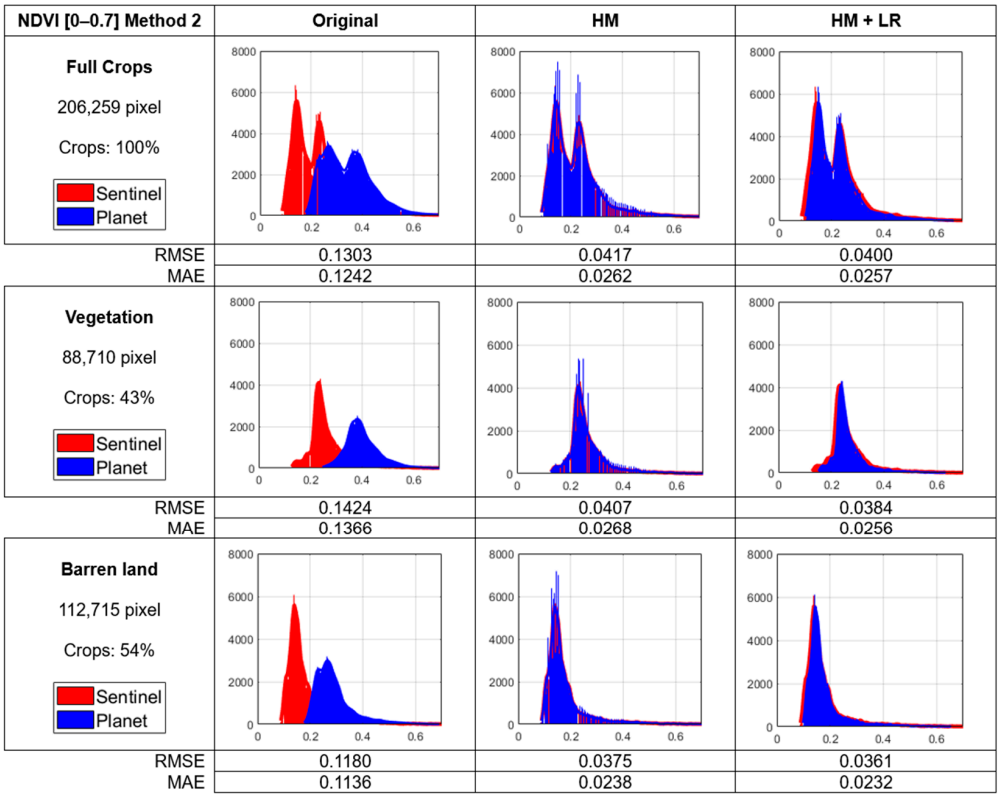

Figure 7. Method 2 for NDVI—LR after HM is not useful for distribution and statistics.

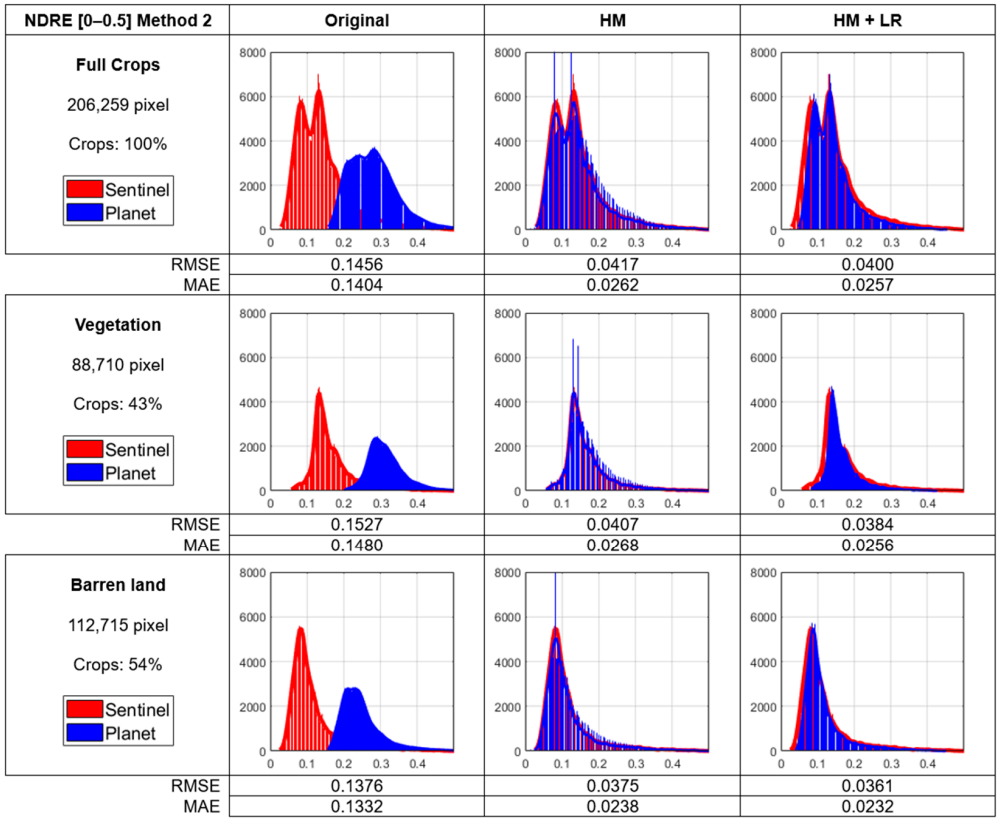

Figure 8. Method 2 for NDRE—LR after HM is not useful for distribution and statistics.

The linear regression statistics can be found in Appendix A

3.5. Key Findings

Henceforth, linear regression shall be abbreviated as LR, histogram shifting as HS, and histogram matching as HM.

- LR alone is not sufficient for image intercalibration as it leaves a shift in the index values, resulting in inaccurate measurements.
- The combination of LR and HS provides a good balance between speed and accuracy.
- HS helps to align the peaks of the histogram of the calibrated image with those of the reference image, reducing the shift left by LR.
- The sequence of LR, HS, and HM results in an overlapping index distribution for NDVI. This means that the calibrated image has a very similar distribution of index values as the reference image, indicating excellent intercalibration results. For NDRE, the overlap is slightly less, but still very high.
- HM is recommended for speed if there is no need to further reduce the error. HM directly matches the histogram of the calibrated image to that of the reference image, ensuring that the overall variability in the index is maintained.
- The combination of HM and LR offers no further advantage over HM alone. LR does not provide any additional alignment benefit once HM has been applied.
- Calibrated NDVI and NDRE have superimposable peaks of vegetation and barren land. These peaks correspond to areas with high and low vegetation density, respectively. With NDVI, the peaks of vegetation and barren land are much more evident compared to NDRE. This is because NDVI is more sensitive to changes in vegetation density than NDRE.
- In Sentinel-2 imagery, the peaks are still evident in NDRE, but less so in PlanetScope. However, after intercalibration it is possible to see the peaks more clearly in both Sentinel-2 and PlanetScope imagery.
- In every application of HM, it is evident that there are PlanetScope histogram peaks that overlay the Sentinel-2 histogram. This phenomenon can be attributed to the impact of the importing of Sentinel-2's variability on PlanetScope. As a result, PlanetScope acquires higher variability over approximately nine pixels embedded within a single Sentinel-2 pixel, which maintains a constant value.
- Despite disparate starting points, the Normalized Difference Vegetation Index (NDVI) and the Normalized Difference Red Edge Index (NDRE) exhibit robust performance after intercalibration. This also happens with the preliminary harmonization of bands influencing NDVI (red and NIR) and the exclusion of the red edge band, which influences the NDRE while incorporating the harmonized NIR band.

4. Discussion

4.1. Interpretation of Results

Following the testing of multiple approaches, the SkySat crop classification detailed in this paper achieved a 97% success rate in identifying rice crops, which were further categorized into vegetation and barren land subclasses. The bimodal histogram for entire crop fields was successfully divided, aligning with the agronomist's reports of sparse vegetation growth during this period. The radiometric intercalibration results were not affected by the masks, implying they can be used across all classes. Thus, applying radiometric intercalibration to these masks demonstrates that intercalibration can be performed regardless of vegetation presence. The classification obtained from the SkySat image and used for PlanetScope/Sentinel-2 intercalibration demonstrated that there is a minimal discrepancy between the root-mean-square error (RMSE) and the mean absolute error (MAE) computed for the three masks (and respective classes). These results also provide evidence that the slightly higher RMSE (between Sentinel-2 and PlanetScope) for the vegetation mask is insignificant in comparison to the miscalibration observed in prior research [14,15]. Intercalibration method 1 for Sentinel-2 and PlanetScope uses linear regression to scale the histogram, aligns the means, and then, matches the histogram to obtain a similar index distribution. This approach is highly accurate but time consuming and resource intensive.

Histogram matching, even when employed independently (method 2), is a robust tool that enables the alignment of responses between various sensors. It is a swift process that preserves the sensor's inherent variability (method 2), thereby eliminating the need for subsequent linear regression. The selection of an appropriate intercalibration methodology is influenced by several critical factors that determine the suitability of each technique; the availability of computational resources by workstations is another important consideration. Workstations with faster processing capabilities may be able to handle more complex intercalibration procedures in a shorter time frame compared to slower workstations. Method 1 could be employed in scenarios where an accurate analysis is required. Additionally, factors such as the availability of resources, cost considerations, and the expertise of the personnel performing the intercalibration may influence the selection of the methodology. Although PlanetScope harmonizes with Sentinel-2 using only the red, green, blue, and NIR bands, these intercalibrations allow for consistent conditions for both the NDVI and NDRE indices. This solution addresses the issue of the PlanetScope red edge band not being harmonized.

Previous research showed that histogram matching was effective in combining PlanetScope and Sentinel-2 data over RGB bands [137]. This paper further demonstrates its capability in calibrating vegetative indices. Method 1 enhances intercalibration by sequentially employing well-known techniques that are typically used in isolation: linear regression, histogram shifting, and histogram matching [137,138]. This paper also demonstrates that integrating linear regression and histogram matching, supplemented by histogram shifting in the proposed sequence, produces superior outcomes.

4.2. Implications

The authors are exploring PlanetScope imagery to create vigor maps, which will help agronomists develop prescription maps for rice. The SkySat image utilized was specifically accessible over "Riserva San Massimo" during a partnership between the University of Pavia and Planet Labs. Currently, its high cost makes it impractical for use in precision farming and limits its utility to research organizations. Agronomists at Riserva San Massimo are eager to evaluate NDVI and NDRE using PlanetScope due to its superior resolution and daily revisit time compared to Sentinel-2, complementing their drone data acquisitions. The purpose of the paper is to demonstrate that irregular vegetation does not affect intercalibration (through SkySat classification), and it introduces two methods for radiometric intercalibration that support this claim. These intercalibration methods are currently used to evaluate the results from different sensors to identify differences and improvements. The research is crucial for agronomists seeking a more cost-effective switch from expensive drones to satellite remote sensing, as it demonstrates two reliable intercalibration methods. The detailed methodologies and case studies presented in this work equip agronomists and drone operators with the knowledge and tools necessary to successfully integrate satellite remote sensing into their operations. Additionally, this research is beneficial for academic institutions and research organizations focused on remote sensing, offering an extensive summary of recent progress in integrating multisource satellite data and its practical uses. Understanding the strengths and limitations of Sentinel-2 and PlanetScope imagery intercalibration, and their fusion, enables decision-makers to create better policies and strategies that leverage these technologies for various environmental and societal challenges, beyond just precision agriculture.

4.3. Limitations

SkySat imagery, characterized by its substantial financial outlay, presents a unique opportunity for universities and research institutions to harness its capabilities at a reduced cost. However, its accessibility for farmers and industry remains limited, posing a significant challenge. The insights provided by this endeavor encompass a comprehensive overview that is often elusive for individuals and farmers alike. This study is specifically presented for dates surrounding the unique SkySat imagery that is available. Intercalibra-

tion assessments conducted for these PlanetScopePlanetScope and Sentinel-2 dates at a four-day interval during the most challenging time frame can be utilized over alternative time frames, where the disparity between the acquisitions of the two sensors is lower (as demonstrated in previous research) [14,15]. Another limitation is the lack of ground validation since the archive was accessible only two years after acquisition. However, classification is validated through an agronomists' experience and bimodal histograms that correctly separate vegetation and barren land into two rice subclasses.

5. Conclusions

5.1. Main Findings

Before intercalibration, the SkySat classification was independently confirmed using histograms: the bimodal histogram correctly separated into NDVI and NDRE, with lower values indicating barren land and higher values representing vegetation. The uneven spatial distribution of rice growth does not greatly affect the seasonal miscalibration between Sentinel-2 and PlanetScope satellites. This is significant because it means intercalibration is possible despite uneven vegetation, and seasonal miscalibration can be corrected using the described methods (1 for accuracy, 2 for speed). Although red edge PlanetScope is not harmonized with Sentinel-2, these methodologies allow NDRE to be accurately calibrated. Within the context of this research endeavor, it is demonstrated that the intercalibration of both indices can be effectively accomplished within the most challenging temporal framework through the methodologies described.

5.2. Future Perspectives

The research is broadening with intercalibrations for 2021, 2022, and 2023, significantly deepening the understanding of "Riserva San Massimo" Rice Farm, even though there are no other SkySat images available, which makes this study unique. This investigation also seeks to reduce edge effects and calibrate PlanetScope images against Sentinel-2, aiming to assess the effectiveness and reliability of these techniques in Precision Agriculture over the given period.

Author Contributions: Conceptualization, C.M.B. and V.M.C.; methodology, C.M.B. and V.M.C.; software, C.M.B.; validation, C.M.B.; formal analysis, C.M.B.; investigation, C.M.B. and V.M.C.; resources, V.M.C.; data curation, C.M.B. and V.M.C.; writing—original draft preparation, C.M.B.; visualization, C.M.B.; supervision, V.M.C.; project administration, V.M.C.; funding acquisition, V.M.C. All authors have read and agreed to the published version of the manuscript.

Funding: This research was funded as part of a doctoral position funded by the PON DM 1061 call.

Data Availability Statement: The original contributions presented in the study are included in the article, further inquiries can be directed to the corresponding author.

Acknowledgments: The authors thank Agr. G. L. Rognoni and Ing. C. Bergonzi for their contributions in choosing the test site and in interpreting field data through their experience, gained through a long collaboration with "Ente Nazionale Risi". The authors thank the "Riserva San Massimo" owners and workers for their support in sharing their experience during field work.

Conflicts of Interest: The authors declare no conflicts of interest.

Appendix A

This appendix augments comprehension of the research by presenting linear regression outcomes derived from MATLAB [214].

The figures and statistics illustrate the efficacy of the processes, elucidated through histograms, thereby enhancing understanding of the research.

Interestingly, the R^2 is slightly lower for vegetation than barren land, suggesting that some hybrid pixels of vegetation and barren land were likely classified as vegetation (like the edge effect).

Linear regression differs significantly between method 1 and method 2. In method 2, linear regression is conducted following histogram matching, which aligns the index values, whereas in method 1, the PlanetScope indices still exhibit higher values than those of Sentinel-2.

The statistics for the linear regression model step used for the NDVI intercalibration in method 1 are presented in Figure A1 (full crops), Figure A2 (vegetation), and Figure A3 (barren land).

In each subsequent graph, the linear regression equation uses "*" as the multiplication sign, following Matlab convention.

Statistics for linear regression model step used for NDRE intercalibration in method 1 are presented in Figure A4 (Full Crops), Figure A5 (Vegetation) and Figure A6 (Barren land).

The statistics for the linear regression model step used for the NDVI intercalibration in method 2 are presented in Figure A7 (full crops), Figure A8 (vegetation), and Figure A9 (barren land).

The statistics for the linear regression model step used for the NDRE intercalibration in method 2 are presented in Figure A10 (full crops), Figure A11 (vegetation), and Figure A12 (barren land).

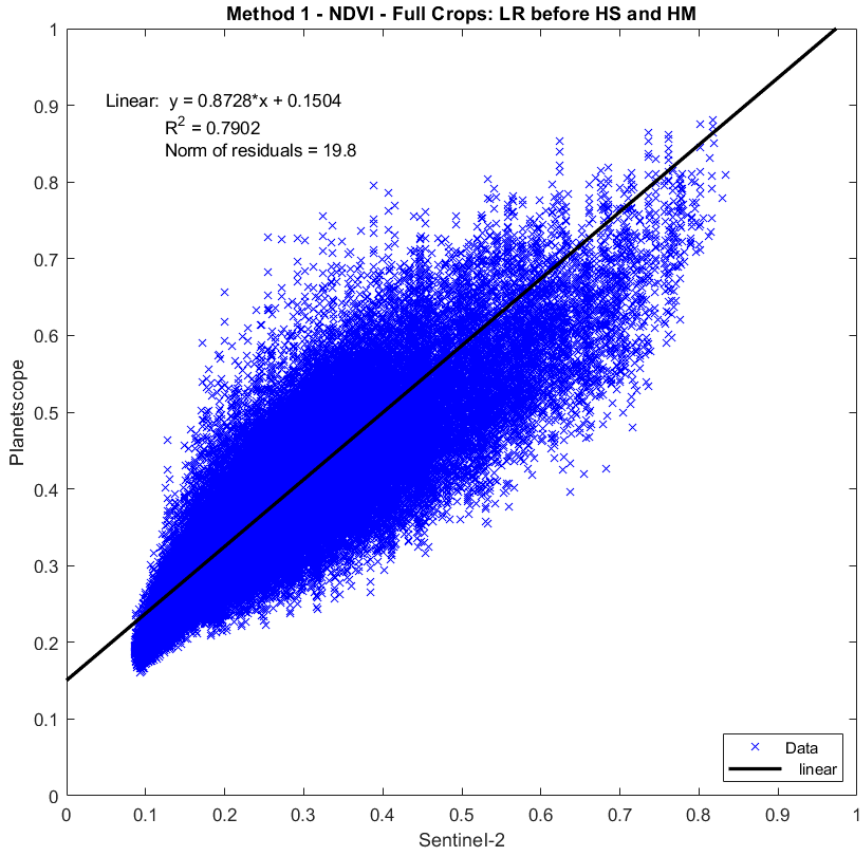

Figure A1. Method 1 for NDVI—linear regression for full crops.

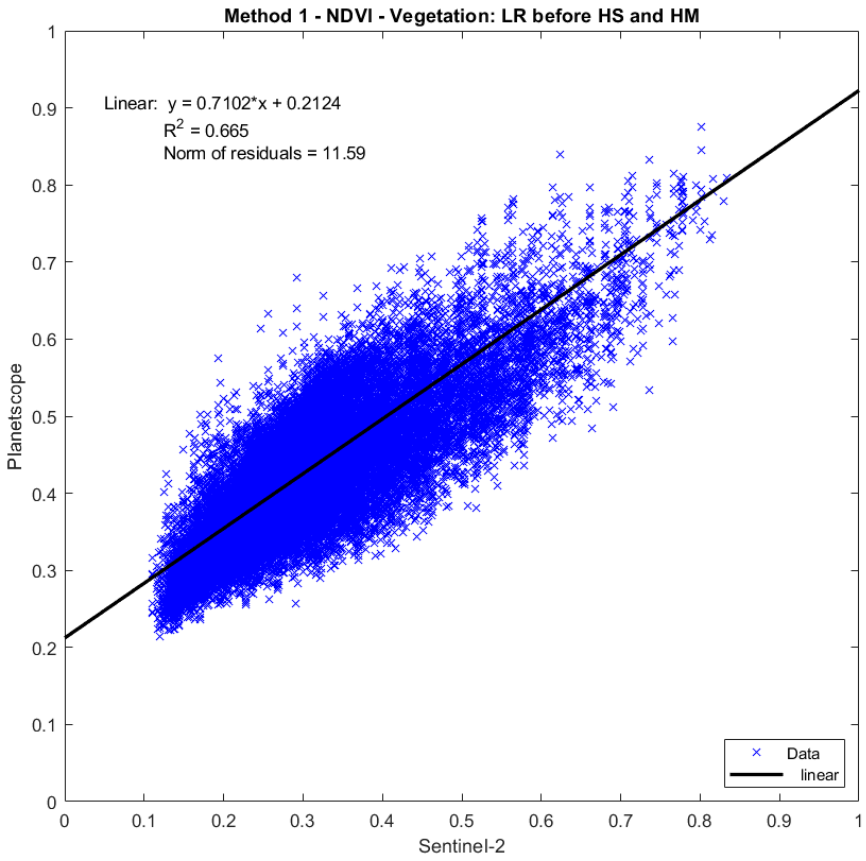

Figure A2. Method 1 for NDVI—linear regression for vegetation subclass.

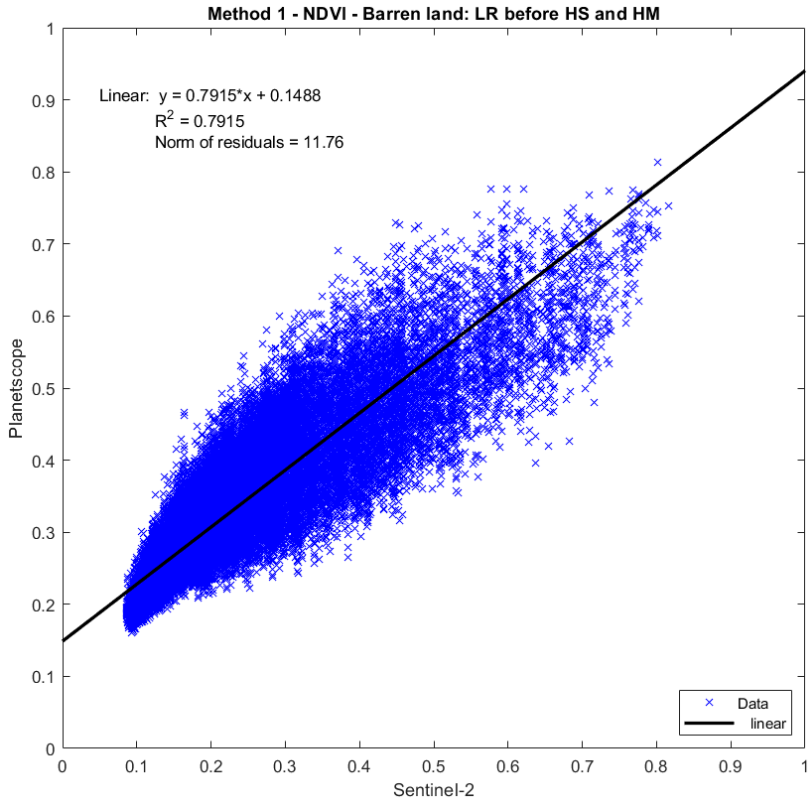

Figure A3. Method 1 for NDVI—linear regression for barren land subclass.

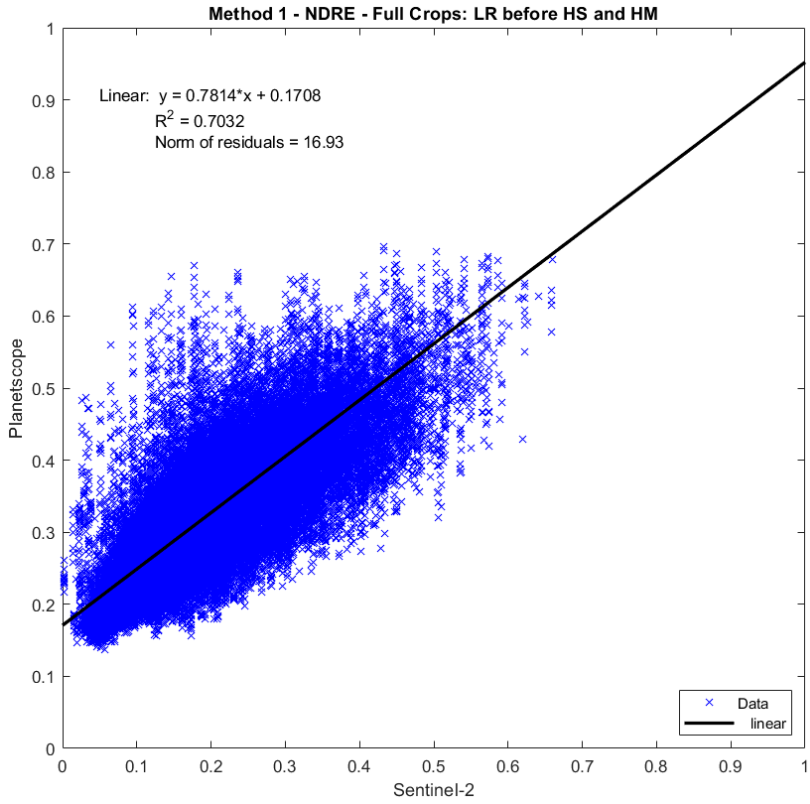

Figure A4. Method 1 for NDRE—linear regression for full crops.

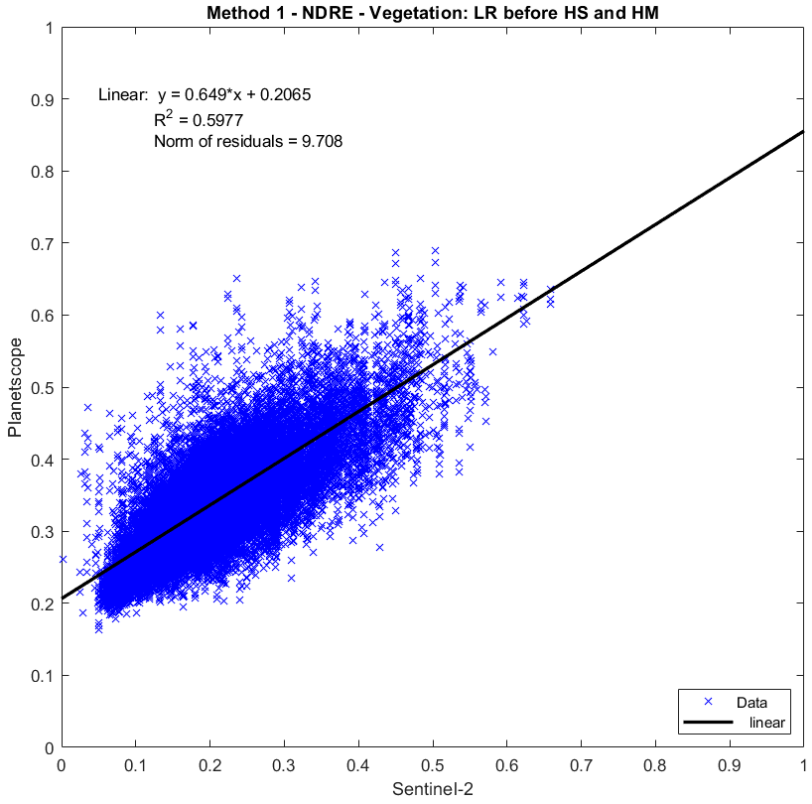

Figure A5. Method 1 for NDRE—linear regression for vegetation subclass.

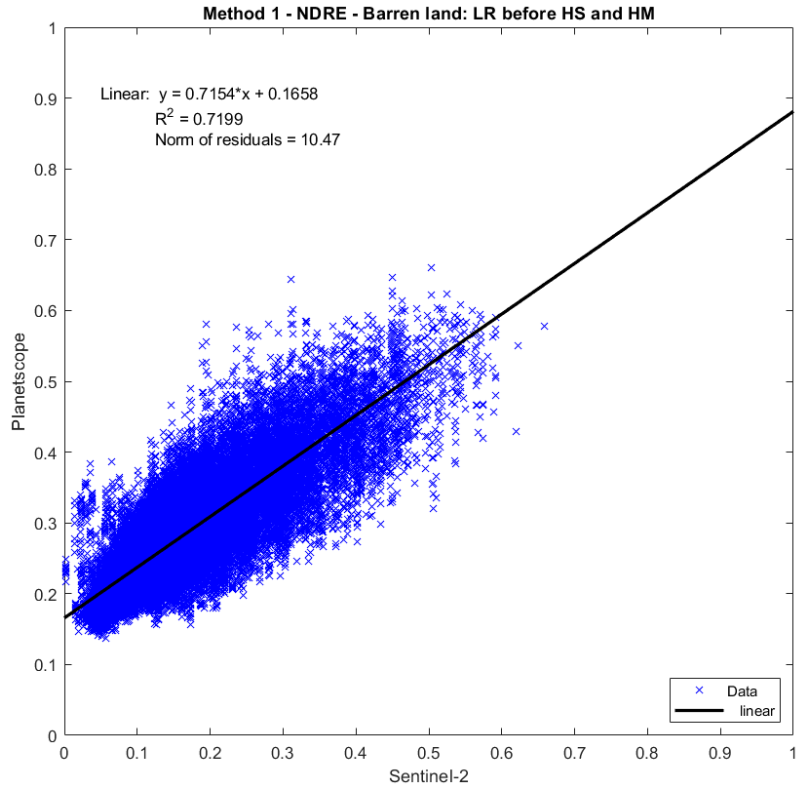

Figure A6. Method 1 for NDRE—linear regression for barren land subclass.

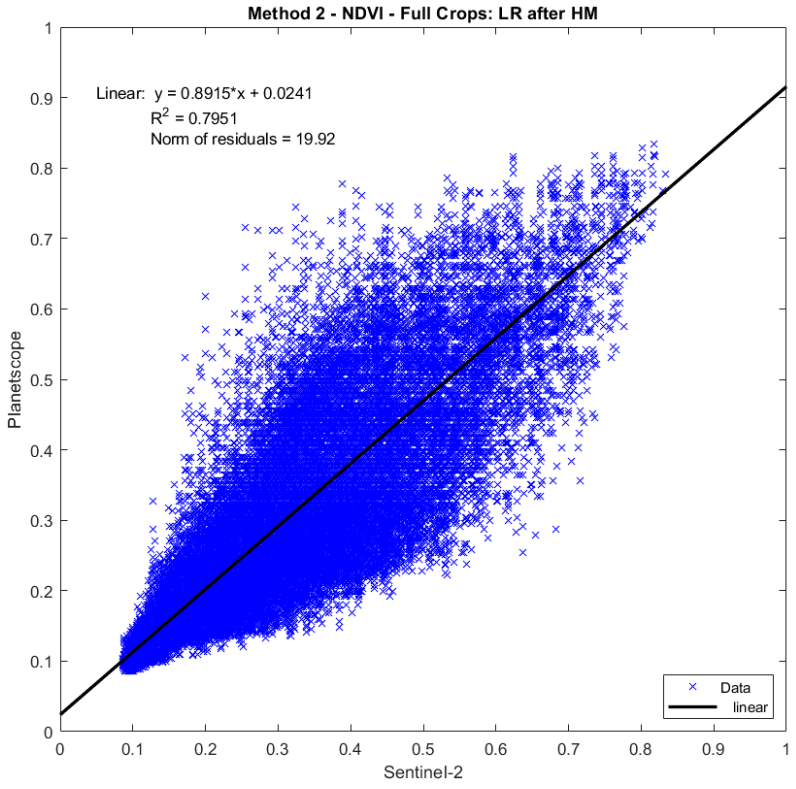

Figure A7. Method 2 for NDVI—linear regression for full crops.

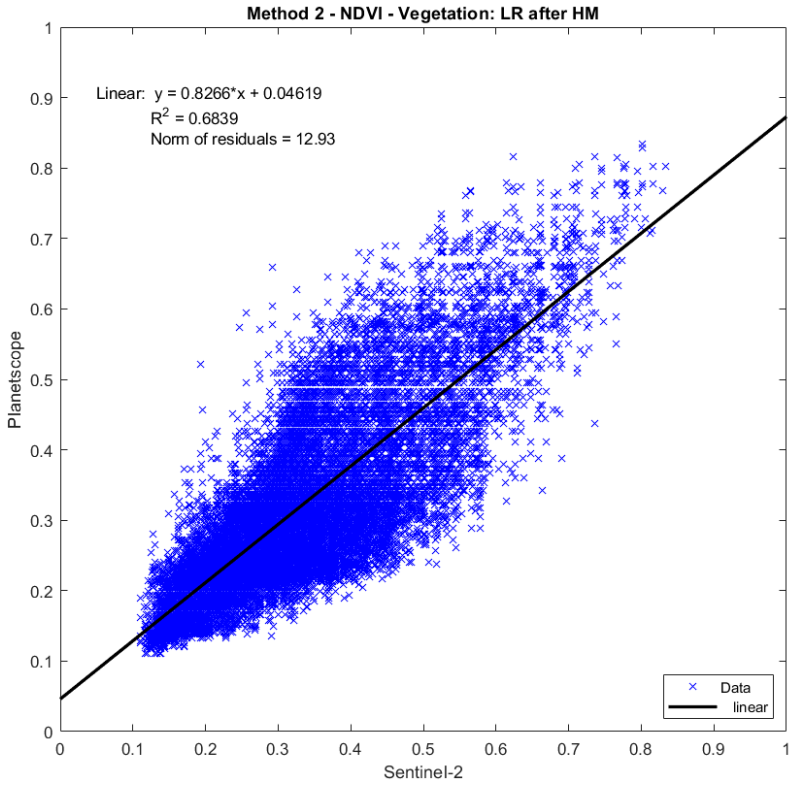

Figure A8. Method 2 for NDVI—linear regression for vegetation subclass.

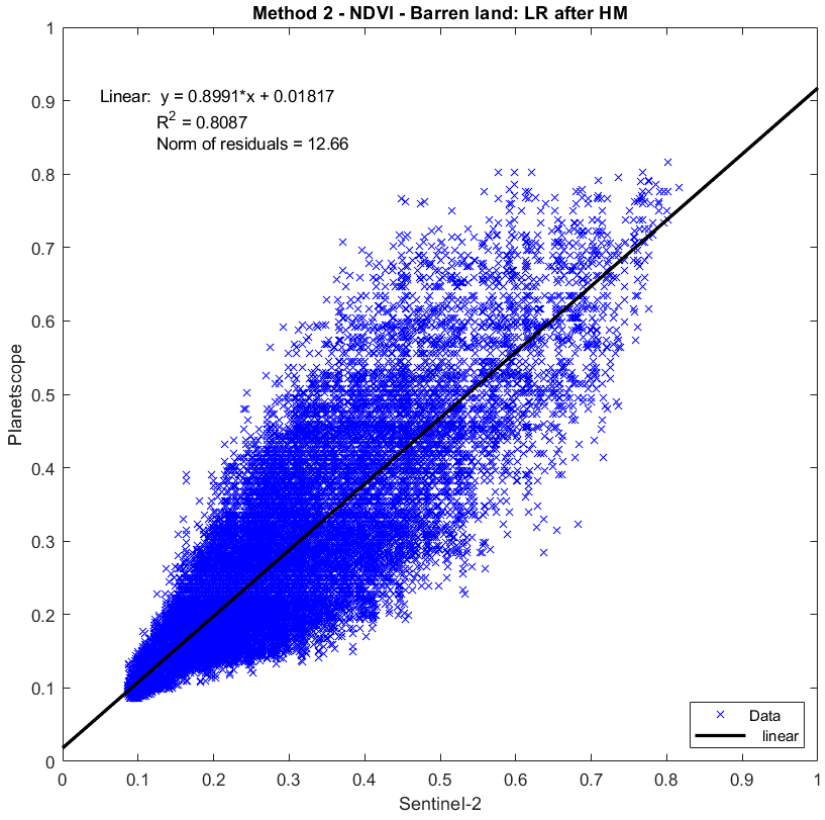

Figure A9. Method 2 for NDVI—linear regression for barren land subclass.

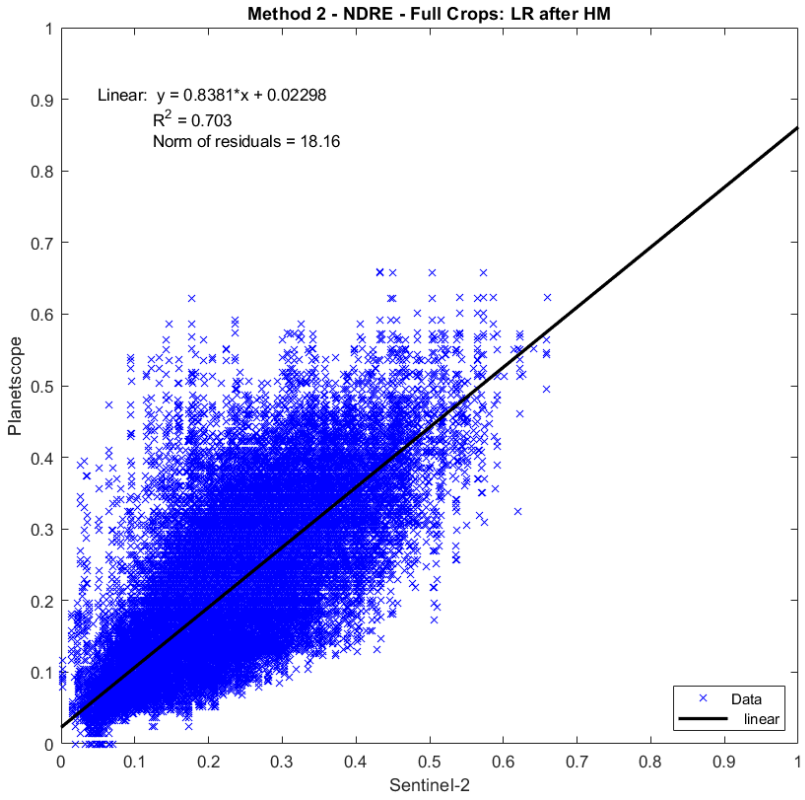

Figure A10. Method 2 for NDRE—linear regression for full crops.

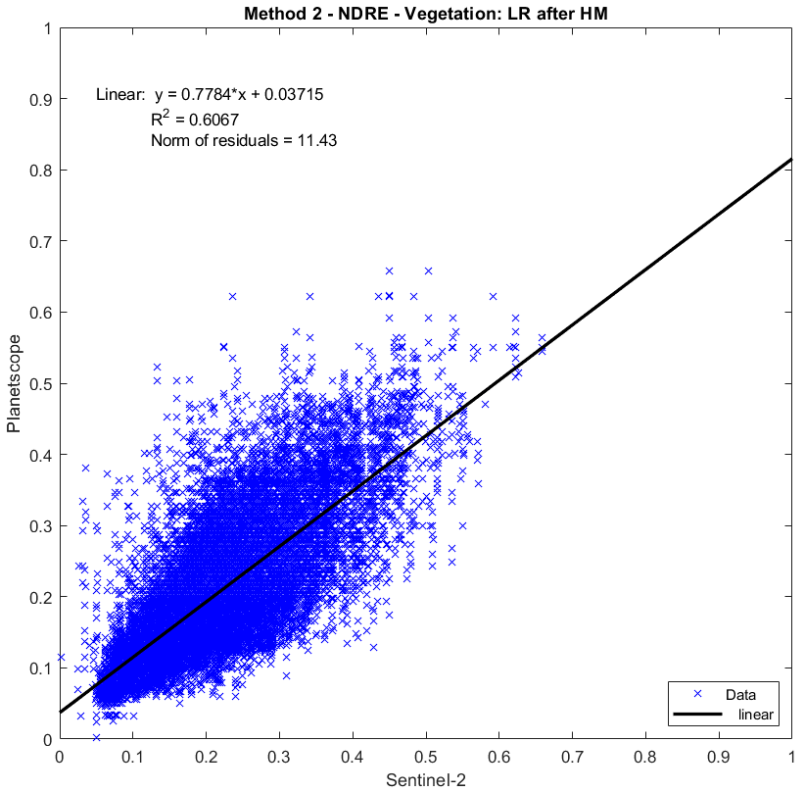

Figure A11. Method 2 for NDRE—linear regression for vegetation subclass.

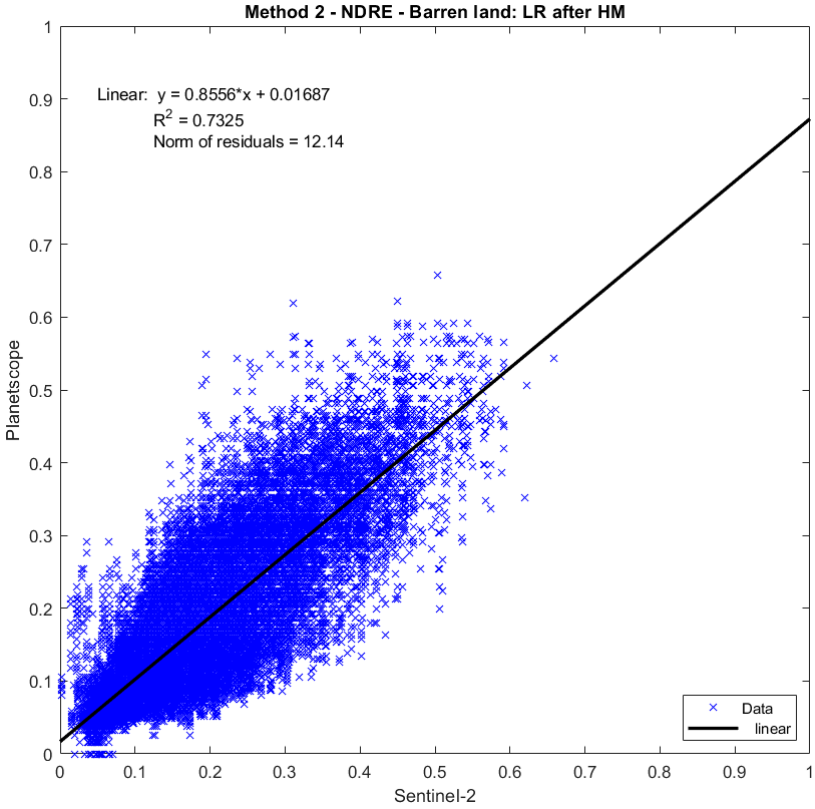

Figure A12. Method 2 for NDRE—linear regression for barren land subclass.

References

1. Paolo Carrà The Italian Rice Is Not a Commodity. Available online: https://www.europarl.europa.eu/cmsdata/148142/Carra_presentation-en.pdf (accessed on 6 October 2024).
2. Rice—FAO—Food and Agriculture Organization of the United Nations. Available online: https://www.fao.org/markets-and-trade/commodities/rice/en/ (accessed on 6 October 2024).
3. Rice Explorer—USDA Foreign Agricultural Service. Available online: https://ipad.fas.usda.gov/cropexplorer/cropview/comm_chartview.aspx?ftypeid=47&fattributeid=1&fctypeid=24&fcattributeid=1&regionid=europe&cntryid=EUE&&cropid=0422110&nationalgraph=false&sel_year=2021&startrow=1 (accessed on 6 October 2024).
4. Europe: Rice Production—USDA Foreign Agricultural Service. Available online: https://ipad.fas.usda.gov/rssiws/al/crop_production_maps/Europe/EU_Rice.png (accessed on 6 October 2024).
5. Rice—Fact Sheet—Agridata European Commission. Available online: https://agriculture.ec.europa.eu/system/files/2019-02/factsheet-eu-rice-market_en_0.pdf (accessed on 6 October 2024).
6. Rice Production Dashboard—Agridata European Commission. Available online: https://agridata.ec.europa.eu/extensions/DashboardRice/RiceProduction.html# (accessed on 6 October 2024).
7. Rice—Agridata European Commission. Available online: https://agridata.ec.europa.eu/extensions/DataPortal/rice.html (accessed on 6 October 2024).
8. Rice Production In Italy. Available online: https://www.sustainableeurice.eu/european-rice/rice-production-in-italy/ (accessed on 1 October 2024).
9. Arcieri, M.; Ghinassi, G. Rice Cultivation in Italy under the Threat of Climatic Change: Trends, Technologies and Research Gaps. *Irrig. Drain.* **2020**, *69*, 517–530. [CrossRef]
10. Ente Nazionale Risi. Available online: https://www.enterisi.it/servizi/notizie/notizie_homepage.aspx (accessed on 9 October 2024).
11. Spiaggiari, O. Risotto Crisis: The Fight to Save Italy's Beloved Dish from Extinction. Available online: https://www.theguardian.com/environment/2024/feb/29/risotto-crisis-the-fight-to-save-italys-beloved-dish-from-extinction-aoe (accessed on 1 October 2024).
12. Varetti, G. *L'almanacco Del Riso 2023: Le Più Importanti News 2022 Di Risoitaliano.Eu*, Risoitaliano.eu.; Indipendently published. 2023.
13. Varetti, G. *L'almanacco Del Riso 2024: Le Più Importanti News 2023 Di Risoitaliano.Eu*, Risoitaliano.eu.; Independently published. 2023.

14. Baldin, C.M.; Casella, V.M. Comparison Between the Vegetation Indices Obtained from Sentinel-2 and Planet: A Case Study over a Rice Farm in Northern Italy. *Commun. Comput. Inf. Sci.* **2024**, *2088*, 257–284. [CrossRef]
15. Baldin, C.M.; Rocca, M.T.; Franzini, M.; Casella, V.M. L'uso Di Immagini Planet Nell'agricoltura Di Precisione: Una Prima Sperimentazione Relativa al Riso. In Proceedings of the Intersezioni Disciplinare—Convegno Sifet 2023, Arezzo, Italy, 27 September 2023.
16. Miniotti, E.; Tenni, D.; Beltarre, G.; Sacco, D.; Rognoni, G.; Finzi, A.; Sgrelli, S.; Bergonzi, C.; Romani, M. Riso, Sensori Ottici e Droni per Ottimizzare La Concimazione. *Terra E Vita* **2015**, *15*, 62–64.
17. Tenni, D.; Rognoni, G.; Finzi, A.; Bergonzi, C.; Sgrelli, S.; Sacco, D.; Miniotti, E.; Beltarre, G.; Romani, M. Concimazione Azotata Di Precisione in Risaia. In Proceedings of the Conferenza ESRI Italia 2019, Rome, Italy, 10–11 April 2019.
18. Miguez, F.E.; Poffenbarger, H. How Can We Estimate Optimum Fertilizer Rates with Accuracy and Precision? *Agric. Environ. Lett.* **2022**, *7*, e20075. [CrossRef]
19. Gebbers, R.; Adamchuk, V.I. Precision Agriculture and Food Security. *Science* **2010**, *327*, 828–831. [CrossRef]
20. He, L. Variable Rate Technologies for Precision Agriculture. In *Encyclopedia of Smart Agriculture Technologies*; Springer: Berlin/Heidelberg, Germany, 2022; pp. 1–9. [CrossRef]
21. Segarra, J.; Buchaillot, M.L.; Araus, J.L.; Kefauver, S.C. Remote Sensing for Precision Agriculture: Sentinel-2 Improved Features and Applications. *Agronomy* **2020**, *10*, 641. [CrossRef]
22. Giuliana, V.; Lucia, M.; Marco, R.; Simone, V. Environmental Life Cycle Assessment of Rice Production in Northern Italy: A Case Study from Vercelli. *Int. J. Life Cycle Assess.* **2024**, *29*, 1523–1540. [CrossRef]
23. La Concimazione Di Precisione in Risicoltura. Facciamo Il Punto—Agrimeccanica—AgroNotizie. Available online: https://agronotizie.imagelinenetwork.com/agrimeccanica/2018/09/04/la-concimazione-di-precisione-in-risicoltura-facciamo-il-punto/59707 (accessed on 31 July 2024).
24. Young, S.L.; Meyer, G.E.; Woldt, W.E. *Future Directions for Automated Weed Management in Precision Agriculture. Automation: The Future of Weed Control in Cropping Systems*; UNL: Lincoln, NE, USA, 2014; pp. 249–259. [CrossRef]
25. Vijayakumar, V.; Ampatzidis, Y.; Schueller, J.K.; Burks, T. Smart Spraying Technologies for Precision Weed Management: A Review. *Smart Agric. Technol.* **2023**, *6*, 100337. [CrossRef]
26. Kamienski, C.; Soininen, J.P.; Taumberger, M.; Dantas, R.; Toscano, A.; Cinotti, T.S.; Maia, R.F.; Neto, A.T. Smart Water Management Platform: IoT-Based Precision Irrigation for Agriculture. *Sensors* **2019**, *19*, 276. [CrossRef]
27. Monteiro, A.; Santos, S. Sustainable Approach to Weed Management: The Role of Precision Weed Management. *Agronomy* **2022**, *12*, 118. [CrossRef]
28. Kovalev, I.V.; Testoyedov, N.A. Modern Unmanned Aerial Technologies for the Development of Agribusiness and Precision Farming. *IOP Conf. Ser. Earth Environ. Sci.* **2020**, *548*, 52080. [CrossRef]
29. Sona, G.; Passoni, D.; Pinto, L.; Pagliari, D.; Masseroni, D.; Ortuani, B.; Facchi, A. UAV multispectral survey to map soil and crop for precision farming applications. *Int. Arch. Photogramm. Remote Sens. Spat. Inf. Sci.* **2016**, *XLI-B1*, 1023–1029. [CrossRef]
30. Filippo, S.; De Petris, S.; Orusa, T.; Borgogno-Mondino, E. MAIA S2 Versus Sentinel 2: Spectral Issues and Their Effects in the Precision Farming Context. In Proceedings of the Computational Science and Its Applications–ICCSA 2021; Osvaldo, G., Murgante, B., Misra, S., Garau, C., Blečić, I., Taniar, D., Bernady, A.O., Rocha, A.M.A.C., Tarantino, E., Torre, C.M., Eds.; Springer International Publishing: Cham, Switzerland, 2021; pp. 63–77.
31. Nutini, F.; Confalonieri, R.; Paleari, L.; Pepe, M.; Criscuolo, L.; Porta, F.; Ranghetti, L.; Busetto, L.; Boschetti, M. Supporting Operational Site-specific Fertilization in Rice Cropping Systems with Infield Smartphone Measurements and Sentinel-2 Observations. *Precis. Agric.* **2021**, *22*, 1284–1303. [CrossRef]
32. Pettersson, C.-G.; Söderström, M.; Eckersten, H. Canopy Reflectance, Thermal Stress, and Apparent Soil Electrical Conductivity as Predictors of within-Field Variability in Grain Yield and Grain Protein of Malting Barley. *Precis. Agric.* **2006**, *7*, 343–359. [CrossRef]
33. Bossung, C.; Schlerf, M.; Machwitz, M. Estimation of Canopy Nitrogen Content in Winter Wheat from Sentinel-2 Images for Operational Agricultural Monitoring. *Precis. Agric.* **2022**, *23*, 2229–2252. [CrossRef]
34. Chang, C.L.; Lin, K.M. Smart Agricultural Machine with a Computer Vision-Based Weeding and Variable-Rate Irrigation Scheme. *Robotics* **2018**, *7*, 38. [CrossRef]
35. Späti, K.; Huber, R.; Finger, R. Benefits of Increasing Information Accuracy in Variable Rate Technologies. *Ecol. Econ.* **2021**, *185*, 107047. [CrossRef]
36. Yang, M.; Xu, X.; Li, Z.; Meng, Y.; Yang, X.; Song, X.; Yang, G.; Xu, S.; Zhu, Q.; Xue, H. Remote Sensing Prescription for Rice Nitrogen Fertilizer Recommendation Based on Improved NFOA Model. *Agronomy* **2022**, *12*, 1804. [CrossRef]
37. Shi, Y.; Cheng, X.; Xi, X.; Weng, W.; Zhang, B.; Zhang, J.; Zhang, R. Effects of a Novel Weeding and Fertilization Scheme on Yield and Quality of Rice. *Agronomy* **2023**, *13*, 2269. [CrossRef]
38. Yu, F.; Bai, J.; Jin, Z.; Zhang, H.; Guo, Z.; Chen, C. Research on Precise Fertilization Method of Rice Tillering Stage Based on UAV Hyperspectral Remote Sensing Prescription Map. *Agronomy* **2022**, *12*, 2893. [CrossRef]
39. Gu, Z.; Zeng, Z.; Shi, X.; Yu, D.; Zheng, W.; Zhang, Z.; Hu, Z. Estimating Models of Vegetation Fractional Coverage Based on Remote Sensing Images at Different Radiometric Correction Levels. *Front. For. China* **2009**, *4*, 402–408. [CrossRef]
40. Soriano-González, J.; Angelats, E.; Martínez-Eixarch, M.; Alcaraz, C. Monitoring Rice Crop and Yield Estimation with Sentinel-2 Data. *Field Crops Res.* **2022**, *281*, 108507. [CrossRef]

41. Najafi, P.; Eftekhari, A.; Sharifi, A. Evaluation of Time-Series Sentinel-2 Images for Early Estimation of Rice Yields in South-West of Iran. *Aircr. Eng. Aerosp. Technol.* **2023**, *95*, 741–748. [CrossRef]
42. Vizzari, M.; Santaga, F.; Benincasa, P. Sentinel 2-Based Nitrogen VRT Fertilization in Wheat: Comparison between Traditional and Simple Precision Practices. *Agronomy* **2019**, *9*, 278. [CrossRef]
43. Bonfil, D.J.; Michael, Y.; Shiff, S.; Lensky, I.M. Optimizing Top Dresseing Nitrogen Fertilization Using Venμs and Sentinel-2 L1 Data. *Remote Sens.* **2021**, *13*, 3934. [CrossRef]
44. Santaga, F.; Benincasa, P.; Vizzari, M. Using Sentinel 2 Data to Guide Nitrogen Fertilization in Central Italy: Comparison Between Flat, Low VRT and High VRT Rates Application in Wheat. *Lect. Notes Comput. Sci. (Incl. Subser. Lect. Notes Artif. Intell. Lect. Notes Bioinform.)* **2020**, *12253*, 78–89. [CrossRef]
45. Ranghetti, L.; Cardarelli, E.; Boschetti, M.; Busetto, L.; Fasola, M. Assessment of Water Management Changes in the Italian Rice Paddies from 2000 to 2016 Using Satellite Data: A Contribution to Agro-Ecological Studies. *Remote Sens.* **2018**, *10*, 416. [CrossRef]
46. Yuan, Y.; Wang, C.; Zai, X.; Song, Y.; Zhang, X. Optimizing Fertilizer Use for Sustainable Food Systems: An Evaluation of Integrated Water-Fertilizer System Adoption among Cotton Farmers in China. *Front. Sustain. Food Syst.* **2023**, *7*, 1310426. [CrossRef]
47. Babcock, B.A. The Effects of Uncertainty on Optimal Nitrogen Applications. *Rev. Agric. Econ.* **1992**, *14*, 271. [CrossRef]
48. Huang, S.; Miao, Y.; Yuan, F.; Gnyp, M.L.; Yao, Y.; Cao, Q.; Wang, H.; Lenz-Wiedemann, V.I.S.; Bareth, G. Potential of RapidEye and WorldView-2 Satellite Data for Improving Rice Nitrogen Status Monitoring at Different Growth Stages. *Remote Sens.* **2017**, *9*, 227. [CrossRef]
49. Brinkhoff, J.; Dunn, B.W.; Robson, A.J. Rice Nitrogen Status Detection Using Commercial-Scale Imagery. *Int. J. Appl. Earth Obs. Geoinf.* **2021**, *105*, 102627. [CrossRef]
50. Kumar, V.; Mahajan, G.; Chauhan, B.S. Rice Weeds and Their Management. In *Rice Production Worldwide*; Springer: Berlin/Heidelberg, Germany, 2017; pp. 361–392. [CrossRef]
51. Svizzero, S. Sustainability, Efficiency, and Circularity of Weedy Rice Management Strategies. *Circ. Econ. Sustain.* **2021**, *1*, 1281–1296. [CrossRef]
52. Vidotto, F.; Ferrero, A. Interactions Between Weedy Rice and Cultivated Rice in Italy. *Ital. J. Agron.* **2009**, *4*, 127–136. [CrossRef]
53. López-Granados, F. Weed Detection for Site-Specific Weed Management: Mapping and Real-Time Approaches. *Weed Res.* **2011**, *51*, 1–11. [CrossRef]
54. Chauhan, B.S.; Mahajan, G.; Kumar, V. *Integrated Weed Management in Rice. Recent Advances in Weed Management*; Springer: Berlin/Heidelberg, Germany, 2014; pp. 125–153. [CrossRef]
55. Young, S.L.; Pitla, S.K.; Van Evert, F.K.; Schueller, J.K.; Pierce, F.J. Moving Integrated Weed Management from Low Level to a Truly Integrated and Highly Specific Weed Management System Using Advanced Technologies. *Weed Res.* **2017**, *57*, 1–5. [CrossRef]
56. Thompson, C.R.; Dille, J.A.; Peterson, D.E. Weed Competition and Management in Sorghum. In *Sorghum*; John Wiley & Sons, Ltd.: Hoboken, NJ, USA, 2019; pp. 347–360, ISBN 9780891186281.
57. Weed Management—IRRI Rice Knowledge Bank. Available online: http://www.knowledgebank.irri.org/step-by-step-production/growth/weed-management (accessed on 31 July 2024).
58. Williams, B.J.; Miller, D.K. Cool-Season Weed Response to Flumioxazin. *Crop Manag.* **2007**, *6*, 1–7. [CrossRef]
59. Gerhards, R.; Andújar Sanchez, D.; Hamouz, P.; Peteinatos, G.G.; Christensen, S.; Fernandez-Quintanilla, C. Advances in Site-Specific Weed Management in Agriculture—A Review. *Weed Res.* **2022**, *62*, 123–133. [CrossRef]
60. Hunter III, J.E.; Gannon, T.W.; Richardson, R.J.; Yelverton, F.H.; Leon, R.G. Integration of Remote-Weed Mapping and an Autonomous Spraying Unmanned Aerial Vehicle for Site-Specific Weed Management. *Pest. Manag. Sci.* **2020**, *76*, 1386–1392. [CrossRef]
61. Kharel, P.; Devkota, P.; MacDonald, G.; Tillman, B. Evaluating Herbicide Programs for Peanut Response and Weed Control. *Crop Forage Turfgrass Manag.* **2022**, *8*, e20191. [CrossRef]
62. Berti, A.; Bàrberi, P.; Vidotto, F.; Ferrero, A.; Zanin, G. Water Management as a Key Component of Integrated Weed Management. *Ital. J. Agron.* **2006**, *1*, 541–552. [CrossRef]
63. Rosle, R.; Che'ya, N.N.; Ang, Y.; Rahmat, F.; Wayayok, A.; Berahim, Z.; Ilahi, W.F.F.; Ismail, M.R.; Omar, M.H. Weed Detection in Rice Fields Using Remote Sensing Technique: A Review. *Appl. Sci.* **2021**, *11*, 10701. [CrossRef]
64. Benvenuti, S.; Dinelli, G.; Bonetti, A. Germination Ecology of Leptochloa Chinensis: A New Weed in the Italian Rice Agro-Environment. *Weed Res.* **2004**, *44*, 87–96. [CrossRef]
65. Brinkhoff, J.; Hornbuckle, J.; Barton, J.L. Assessment of Aquatic Weed in Irrigation Channels Using UAV and Satellite Imagery. *Water* **2018**, *10*, 1497. [CrossRef]
66. Nelson, K.A.; Renner, K.A. Weed Management in Wide- and Narrow-Row Glyphosate Resistant Soybean. *J. Prod. Agric.* **1999**, *12*, 460–465. [CrossRef]
67. Nagargade, M.; Singh, M.; Tyagi, V. Ecologically Sustainable Integrated Weed Management in Dry and Irrigated Direct-Seeded Rice. *Adv. Plants Agric. Res.* **2018**, *8*, 319–331. [CrossRef]
68. Huang, H.; Deng, J.; Lan, Y.; Yang, A.; Deng, X.; Zhang, L. A Fully Convolutional Network for Weed Mapping of Unmanned Aerial Vehicle (UAV) Imagery. *PLoS ONE* **2018**, *13*, 0196302. [CrossRef]
69. Hamouz, P.; Hamouzová, K.; Holec, J.; Tyšer, L. Impact of Site-Specific Weed Management on Herbicide Savings and Winter Wheat Yield. *Plant Soil Environ.* **2013**, *59*, 101–107. [CrossRef]

70. Pflanz, M.; Nordmeyer, H.; Schirrmann, M. Weed Mapping with UAS Imagery and a Bag of Visual Words Based Image Classifier. *Remote Sens.* **2018**, *10*, 1530. [CrossRef]
71. Cutulle, M.A.; Maja, J.M. Determining the Utility of an Unmanned Ground Vehicle for Weed Control in Specialty Crop Systems. *Ital. J. Agron.* **2021**, *16*. [CrossRef]
72. Huang, H.; Deng, J.; Lan, Y.; Yang, A.; Deng, X.; Wen, S.; Zhang, H.; Zhang, Y. Accurate Weed Mapping and Prescription Map Generation Based on Fully Convolutional Networks Using UAV Imagery. *Sensors* **2018**, *18*, 3299. [CrossRef]
73. Ogwuike, P.; Rodenburg, J.; Diagne, A.; Agboh-Noameshie, A.R.; Amovin-Assagba, E. Weed Management in Upland Rice in Sub-Saharan Africa: Impact on Labor and Crop Productivity. *Food Secur.* **2014**, *6*, 327–337. [CrossRef]
74. Roslim, M.H.M.; Juraimi, A.S.; Che'ya, N.N.; Sulaiman, N.; Manaf, M.N.H.A.; Ramli, Z.; Motmainna, M. Using Remote Sensing and an Unmanned Aerial System for Weed Management in Agricultural Crops: A Review. *Agronomy* **2021**, *11*, 1809. [CrossRef]
75. Peña, J.M.; Torres-Sánchez, J.; de Castro, A.I.; Kelly, M.; López-Granados, F. Weed Mapping in Early-Season Maize Fields Using Object-Based Analysis of Unmanned Aerial Vehicle (UAV) Images. *PLoS ONE* **2013**, *8*, 0077151. [CrossRef] [PubMed]
76. Mudereri, B.T.; Dube, T.; Adel-Rahman, E.M.; Niassy, S.; Kimathi, E.; Khan, Z.; Landmann, T. A Comparative analysis of planetscope and sentinel sentinel-2 space-borne sensors in mapping striga weed using guided regularised random forest classification ensemble. *Int. Arch. Photogramm. Remote Sens. Spat. Inf. Sci.* **2019**, *XLII-2-W13*, 701–708. [CrossRef]
77. Mattivi, P.; Pappalardo, S.E.; Nikolić, N.; Mandolesi, L.; Persichetti, A.; De Marchi, M.; Masin, R. Can Commercial Low-Cost Drones and Open-Source GIS Technologies Be Suitable for Semi-Automatic Weed Mapping for Smart Farming? A Case Study in NE Italy. *Remote Sens.* **2021**, *13*, 1869. [CrossRef]
78. Cordero, E.; Moretti, B.; Miniotti, E.F.; Tenni, D.; Beltarre, G.; Romani, M.; Sacco, D. Fertilisation Strategy and Ground Sensor Measurements to Optimise Rice Yield. *Eur. J. Agron.* **2018**, *99*, 177–185. [CrossRef]
79. Franch, B.; San Bautista, A.; Fita, D.; Rubio, C.; Tarrazó-Serrano, D.; Sánchez, A.; Skakun, S.; Vermote, E.; Becker-Reshef, I.; Uris, A. Within-Field Rice Yield Estimation Based on Sentinel-2 Satellite Data. *Remote Sens.* **2021**, *13*, 4095. [CrossRef]
80. Amankulova, K.; Farmonov, N.; Akramova, P.; Tursunov, I.; Mucsi, L. Comparison of PlanetScope, Sentinel-2, and Landsat 8 Data in Soybean Yield Estimation within-Field Variability with Random Forest Regression. *Heliyon* **2023**, *9*, e17432. [CrossRef]
81. Rehman, T.H.; Lundy, M.E.; Linquist, B.A. Comparative Sensitivity of Vegetation Indices Measured via Proximal and Aerial Sensors for Assessing N Status and Predicting Grain Yield in Rice Cropping Systems. *Remote Sens.* **2022**, *14*, 2770. [CrossRef]
82. Benedetti, R.; Rossini, P. On the Use of NDVI Profiles as a Tool for Agricultural Statistics: The Case Study of Wheat Yield Estimate and Forecast in Emilia Romagna. *Remote Sens. Environ.* **1993**, *45*, 311–326. [CrossRef]
83. Wang, K.; Huggins, D.R.; Tao, H. Rapid Mapping of Winter Wheat Yield, Protein, and Nitrogen Uptake Using Remote and Proximal Sensing. *Int. J. Appl. Earth Obs. Geoinf.* **2019**, *82*, 101921. [CrossRef]
84. Jain, M.; Zhou, W.; Paliwal, A. Mapping Smallholder Yields Using Planet and Sentinel-2 Satellite Data. In *Remote Sensing of Agriculture and Land Cover/Land Use Changes in South and Southeast Asian Countries*; Vadrevu, K.P., Le Toan, T., Ray, S.S., Justice, C.O., Eds.; Springer International Publishing: Cham, Switzerland, 2022; pp. 187–199, ISBN 978-3-030-92365-5.
85. The Yield Response to Nitrogen: Subjective Belief Bias in Nitrogen Management | Agricultural Policy Review. Available online: https://agpolicyreview.card.iastate.edu/spring-2016/yield-response-nitrogen-subjective-belief-bias-nitrogen-management (accessed on 1 August 2024).
86. Hamani, A.K.M.; Abubakar, S.A.; Si, Z.; Kama, R.; Gao, Y.; Duan, A. Responses of Grain Yield and Water-Nitrogen Dynamic of Drip-Irrigated Winter Wheat (*Triticum aestivum* L.) to Different Nitrogen Fertigation and Water Regimes in the North China Plain. *Agric. Water Manag.* **2023**, *288*, 108494. [CrossRef]
87. Farmonov, N.; Amankulova, K.; Szatmári, J.; Urinov, J.; Narmanov, Z.; Nosirov, J.; Mucsi, L. Combining PlanetScope and Sentinel-2 Images with Environmental Data for Improved Wheat Yield Estimation. *Int. J. Digit. Earth* **2023**, *16*, 847–867. [CrossRef]
88. de Lima, I.P.; Jorge, R.G.; de Lima, J.L.M.P. Remote Sensing Monitoring of Rice Fields: Towards Assessing Water Saving Irrigation Management Practices. *Front. Remote Sens.* **2021**, *2*, 762093. [CrossRef]
89. Mallareddy, M.; Thirumalaikumar, R.; Balasubramanian, P.; Naseeruddin, R.; Nithya, N.; Mariadoss, A.; Eazhilkrishna, N.; Choudhary, A.K.; Deiveegan, M.; Subramanian, E.; et al. Maximizing Water Use Efficiency in Rice Farming: A Comprehensive Review of Innovative Irrigation Management Technologies. *Water* **2023**, *15*, 1802. [CrossRef]
90. Sun, J.; Chen, L.; Qi, P.; Zhang, G. Agricultural Irrigation Water Requirement and Its Response to Climatic Factors Based on Remote Sensing and Single Crop Coefficient Method. *Water Resour. Manag.* **2024**, *38*, 5215–5233. [CrossRef]
91. Piñón-Villarrea, A.R.; Samani, Z.A.; Bawazir, A.S.; Bleiweiss, M.P. Correcting the Edge Effect for Sensor Spatial Response in Evapotranspiration Estimation through Remote Sensing. *J. Irrig. Drain. Eng.* **2020**, *146*, 06020004. [CrossRef]
92. Electromagnetic Spectra—An Overview | ScienceDirect Topics. Available online: https://www.sciencedirect.com/topics/earth-and-planetary-sciences/electromagnetic-spectra (accessed on 1 August 2024).
93. Laake, A. *Electromagnetic Spectral Bands Used for Remote Sensing*; Springer: Berlin/Heidelberg, Germany, 2022; pp. 21–35. [CrossRef]
94. Pawan Gupta; Melanie Follette-Cook NASA—Fundamentals of Satellite Remote Sensing. Available online: https://appliedsciences.nasa.gov/sites/default/files/D1P3_Fundamentals.pdf (accessed on 1 August 2024).
95. NASA ARSET—Fundamentals of Remote Sensing. Available online: https://appliedsciences.nasa.gov/sites/default/files/2022-11/Fundamentals_of_RS_Edited_SC.pdf (accessed on 1 August 2024).

96. Vegetation Indices. Available online: https://gsp.humboldt.edu/olm/Courses/GSP_216/lessons/Spectral-Enhancements/NDVI.html (accessed on 31 July 2024).
97. Zeng, Y.; Hao, D.; Huete, A.; Dechant, B.; Berry, J.; Chen, J.M.; Joiner, J.; Frankenberg, C.; Bond-Lamberty, B.; Ryu, Y.; et al. Optical Vegetation Indices for Monitoring Terrestrial Ecosystems Globally. *Nat. Rev. Earth Environ.* **2022**, *3*, 477–493. [CrossRef]
98. Gašparović, M.; Medak, D.; Pilaš, I.; Jurjević, L.; Balenović, I. Fusion of sentinel-2 and planetscope imagery for vegetation detection and monitoring. *Int. Arch. Photogramm. Remote Sens. Spat. Inf. Sci.* **2018**, *XLII–1*, 155–160. [CrossRef]
99. Veneros, J.; Chavez, S.; Oliva, M.; Arellanos, E.; Maicelo, J.L.; García, L. Comparing Six Vegetation Indexes between Aquatic Ecosystems Using a Multispectral Camera and a Parrot Disco-Pro Ag Drone, the ArcGIS, and the Family Error Rate: A Case Study of the Peruvian Jalca. *Water* **2023**, *15*, 3103. [CrossRef]
100. IDB—Index DataBase. Available online: https://www.indexdatabase.de/ (accessed on 31 July 2024).
101. Bannari, A.; Morin, D.; Bonn, F.; Huete, A.R. A Review of Vegetation Indices. *Remote Sens. Rev.* **1995**, *13*, 95–120. [CrossRef]
102. SR. Available online: https://pro.arcgis.com/en/pro-app/latest/arcpy/image-analyst/sr.htm (accessed on 4 October 2024).
103. Band Arithmetic Function. Available online: https://pro.arcgis.com/en/pro-app/latest/help/analysis/raster-functions/band-arithmetic-function.htm (accessed on 4 October 2024).
104. Rouse, J.W., Jr.; Haas, R.H.; Schell, J.A.; Deering, D.W. Monitoring Vegetation Systems in the Great Plains with ERTS. In Proceedings of the NASA, Goddard Space Flight Center 3D ERTS-1 Symp. Sect. A., NASA, Washington, DC, USA, 1 January 1974; Volume 1.
105. Gitelson, A.A.; Kaufman, Y.J.; Stark, R.; Rundquist, D. Novel Algorithms for Remote Estimation of Vegetation Fraction. *Remote Sens. Environ.* **2002**, *80*, 76–87. [CrossRef]
106. Gitelson, A.; Merzlyak, M.N. Quantitative Estimation of Chlorophyll-a Using Reflectance Spectra: Experiments with Autumn Chestnut and Maple Leaves. *J. Photochem. Photobiol. B* **1994**, *22*, 247–252. [CrossRef]
107. Birth, G.S.; McVey, G.R. Measuring the Color of Growing Turf with a Reflectance Spectrophotometer. *Agron. J.* **1968**, *60*, 640–643. [CrossRef]
108. Farbo, A.; Sarvia, F.; De Petris, S.; Borgogno-Mondino, E. Preliminary concerns about agronomic interpretation of ndvi time series from sentinel-2 data: Phenology and thermal efficiency of winter wheat in Piemonte (NW Italy). *Int. Arch. Photogramm. Remote Sens. Spat. Inf. Sci.* **2022**, *XLIII-B3-2022*, 863–870. [CrossRef]
109. Bellón, B.; Bégué, A.; Lo Seen, D.; De Almeida, C.A.; Simões, M. A Remote Sensing Approach for Regional-Scale Mapping of Agricultural Land-Use Systems Based on NDVI Time Series. *Remote Sens.* **2017**, *9*, 600. [CrossRef]
110. Dworak, V.; Selbeck, J.; Dammer, K.H.; Hoffmann, M.; Zarezadeh, A.A.; Bobda, C. Strategy for the Development of a Smart NDVI Camera System for Outdoor Plant Detection and Agricultural Embedded Systems. *Sensors* **2013**, *13*, 1523–1538. [CrossRef]
111. Sruthi, S.; Aslam, M.A.M. Agricultural Drought Analysis Using the NDVI and Land Surface Temperature Data; a Case Study of Raichur District. *Aquat. Procedia* **2015**, *4*, 1258–1264. [CrossRef]
112. Boiarskii, B.; Hasegawa, H. Comparison of NDVI and NDRE Indices to Detect Differences in Vegetation and Chlorophyll Content. *J. Mech. Contin. Math. Sci.* **2019**, *4*, 20–29. [CrossRef]
113. Lenney, M.P.; Woodcock, C.E.; Collins, J.B.; Hamdi, H. The Status of Agricultural Lands in Egypt: The Use of Multitemporal NDVI Features Derived from Landsat TM. *Remote Sens. Environ.* **1996**, *56*, 8–20. [CrossRef]
114. NDRE–Eos Data Analytics. Available online: https://eos.com/industries/agriculture/ndre/ (accessed on 1 February 2024).
115. NDVI, the Foundation for Remote Sensing Phenology | U.S. Geological Survey. Available online: https://www.usgs.gov/special-topics/remote-sensing-phenology/science/ndvi-foundation-remote-sensing-phenology (accessed on 1 August 2024).
116. Voitik, A.; Kravchenko, V.; Pushka, O.; Kutkovetska, T.; Shchur, T.; Kocira, S. Comparison of NDVI, NDRE, MSAVI and NDSI Indices for Early Diagnosis of Crop Problems. *Agric. Eng.* **2023**, *27*, 47–57. [CrossRef]
117. Sharifi, A.; Felegari, S. Remotely Sensed Normalized Difference Red-Edge Index for Rangeland Biomass Estimation. *Aircr. Eng. Aerosp. Technol.* **2023**, *95*, 1128–1136. [CrossRef]
118. Barnes, E.; Clarke, T.R.; Richards, S.E.; Colaizzi, P.; Haberland, J.; Kostrzewski, M.; Waller, P.; Choi, C.; Riley, E.; Thompson, T.L. Coincident Detection of Crop Water Stress, Nitrogen Status, and Canopy Density Using Ground Based Multispectral Data. 2000. Available online: https://www.researchgate.net/publication/43256762_Coincident_detection_of_crop_water_stress_nitrogen_status_and_canopy_density_using_ground_based_multispectral_data (accessed on 9 October 2024).
119. Kriegler, F.J.; Malila, W.A.; Nalepka, R.F.; Richardson, W. Preprocessing Transformations and Their Effects on Multispectral Recognition. In Proceedings of the Remote Sensing of Environment, VI, Ann Arbor, MI, USA, 13–16 January 1969; p. 97.
120. MSAVI2. Available online: https://step.esa.int/main/wp-content/help/versions/10.0.0/snap-toolboxes/eu.esa.opt.opttbx.radiometric.indices.ui/msavi2/Msavi2AlgorithmSpecification.html (accessed on 31 July 2024).
121. Lemenkova, P.; Debeir, O. Computing Vegetation Indices from the Satellite Images Using GRASS GIS Scripts for Monitoring Mangrove Forests in the Coastal Landscapes of Niger Delta, Nigeria. *J. Mar. Sci. Eng.* **2023**, *11*, 871. [CrossRef]
122. Lavender, S.; Lavender, A. *Practical Handbook of Remote Sensing*, 2nd ed.; CRC Press: Boca Raton, FL, USA, 2023.
123. Tassinari, A.A.V.V. *Manuale Dell'Agronomo, Il Nuovo "TASSINARI"*, 6th ed.; Reda Edizioni per l'agricoltura: Brescia, Italy, 2018.
124. Tassinari, A.A.V.V. *Manuale Dell'esame Abilitante Alla Professione Di Agrotecnico e Di Agrotecnico Laureato, Nonché per l'Agronomo, Il Forestale Ed Il Perito Agrario*, 2nd ed.; Società Editoriale Nepenthes: Forlì, Italy, 2021.
125. Ribaudo, F. *Prontuario Di Agricoltura*, 2nd ed.; Hoepli: Milano, Italy, 2021.

126. Tho, L.C.B.; Umetsu, C. Rice Variety and Sustainable Farming: A Case Study in the Mekong Delta, Vietnam. *Environ. Chall.* **2022**, *8*, 100532. [CrossRef]
127. Bekele, I.; Lulie, B.; Habte, M.; Boke, S.; Hailu, G.; Mariam, E.H.; Ahmed, J.S.; Abera, W.; Sileshi, G.W. Response of Maize Yield to Nitrogen, Phosphorus, Potassium and Sulphur Rates on Andosols and Nitisols in Ethiopia. *Exp. Agric.* **2022**, *58*, e11. [CrossRef]
128. Tall and Short Stature Corn Agronomic Response to Nitrogen Rates | Crop Science US. Available online: https://www.cropscience.bayer.us/articles/bayer/corn-response-nitrogen-rates (accessed on 1 August 2024).
129. Zhang, T.; Su, J.; Liu, C.; Chen, W.H.; Liu, H.; Liu, G. Band Selection in Sentinel-2 Satellite for Agriculture Applications. In Proceedings of the ICAC 2017—2017 23rd IEEE International Conference on Automation and Computing: Addressing Global Challenges through Automation and Computing, Huddersfield, UK, 7–8 September 2017. [CrossRef]
130. Zagajewski, B.; Kluczek, M.; Zdunek, K.B.; Holland, D. Sentinel-2 versus PlanetScope Images for Goldenrod Invasive Plant Species Mapping. *Remote Sens.* **2024**, *16*, 636. [CrossRef]
131. Annovazzi-Lodi, L.; Casella, V.; Baldin, C.M.; Bernini, A.; Adeniyi, O.D.; Maerker, M. *Per Un Uso Del Suolo Dinamico: Classificazione Di Serie Storiche Di Immagini Sentinel-2*; ASITA: Genova, Switzerland, 2021.
132. Lijun Wang Yang Bai, J.W.Z.Z.F.Q.; Hu, J. Histogram Matching-Based Semantic Segmentation Model for Crop Classification with Sentinel-2 Satellite Imagery. *GIsci Remote Sens.* **2023**, *60*, 2281142. [CrossRef]
133. Rossi, M.; Candiani, G.; Nutini, F.; Gianinetto, M.; Boschetti, M. Sentinel-2 Estimation of CNC and LAI in Rice Cropping System through Hybrid Approach Modelling. *Eur. J. Remote Sens.* **2023**, *56*, 2117651. [CrossRef]
134. Copernicus Sentinel-2 Leads Precision Farming into New Era—Sentinel Success Stories—Sentinel Online. Available online: https://sentinels.copernicus.eu/web/success-stories/-/copernicus-sentinel-2-leads-precision-farming-into-new-era (accessed on 31 July 2024).
135. Courault, D.; Hossard, L.; Demarez, V.; Dechatre, H.; Irfan, K.; Baghdadi, N.; Flamain, F.; Ruget, F. STICS Crop Model and Sentinel-2 Images for Monitoring Rice Growth and Yield in the Camargue Region. *Agron. Sustain. Dev.* **2021**, *41*, 1–17. [CrossRef]
136. Farbo, A.; Meloni, R.; Blandino, M.; Sarvia, F.; Reyneri, A.; Borgogno-Mondino, E. Spectral Measures from Sentinel-2 Imagery vs Ground-Based Data from Rapidscan© Sensor: Performances on Winter Wheat. In *Proceedings of the Geomatics for Green and Digital Transition*; Enrico, B.-M., Zamperlin, P., Eds.; Springer International Publishing: Cham, Switzerland, 2022; pp. 211–221.
137. Malczewska, A.; Malczewski, J.; Hejmanowska, B. Challenges in preparing datasets for super-resolution on the example of sentinel-2 and planet scope images. *Int. Arch. Photogramm. Remote Sens. Spat. Inf. Sci.* **2023**, *XLVIII-1-W3-2023*, 91–98. [CrossRef]
138. Borgogno-Mondino, E.; Farbo, A.; Novello, V.; Palma, L.d. A Fast Regression-Based Approach to Map Water Status of Pomegranate Orchards with Sentinel 2 Data. *Horticulturae* **2022**, *8*, 759. [CrossRef]
139. Segarra, J.; Buchaillot, M.L.; Stefani, U.; Araus, J.L.; Kefauver, S.C. Sentinel-2 Responsiveness to Fertilization Gradients in Wheat at Field Level in Córdoba Province, Argentina. In Proceedings of the 2020 Mediterranean and Middle-East Geoscience and Remote Sensing Symposium, M2GARSS 2020—Proceedings, Tunis, Tunisia, 9–11 March 2020; pp. 322–325. [CrossRef]
140. Sentinel-2 MSI Instrument. Available online: https://sentinels.copernicus.eu/web/sentinel/technical-guides/sentinel-2-msi/msi-instrument (accessed on 1 February 2024).
141. Sentinel-2 Satellite Overview. Available online: https://sentiwiki.copernicus.eu/web/s2-mission (accessed on 18 October 2024).
142. Sentinel-2 Radiometric Resolution. Available online: https://sentinels.copernicus.eu/en/web/sentinel/missions/sentinel-2/instrument-payload/resolution-and-swath (accessed on 18 October 2024).
143. Sentinel-2 Images the Globe Every 5 Days. Available online: https://sentinel.esa.int/web/success-stories/-/sentinel-2-images-the-globe-every-5-days (accessed on 18 October 2024).
144. Sentinel-2 Product Types. Available online: https://sentiwiki.copernicus.eu/web/s2-products (accessed on 18 October 2024).
145. Sentinel-2C Joins the Copernicus Family in Orbit. Available online: https://www.esa.int/Applications/Observing_the_Earth/Copernicus/Sentinel-2/Sentinel-2C_joins_the_Copernicus_family_in_orbit (accessed on 13 September 2024).
146. Copernicus Sentinel-2 (Processed by ESA), 2021, MSI Level-2A BOA Reflectance Product. Collection 1. European Space Agency. Available online: https://sentinels.copernicus.eu/web/sentinel/sentinel-data-access/sentinel-products/sentinel-2-data-products/collection-1-level-2a (accessed on 18 October 2024).
147. Zhou, G.S.-N.; Lam, N. Reducing Edge Effects in the Classification of High Resolution Imagery. *Photogramm. Eng. Remote Sens.* **2008**, *74*, 431–441. [CrossRef]
148. PlanetScope Overview—Earth Online. Available online: https://earth.esa.int/eogateway/missions/planetscope/description (accessed on 31 July 2024).
149. Vizzari, M. PlanetScope, Sentinel-2, and Sentinel-1 Data Integration for Object-Based Land Cover Classification in Google Earth Engine. *Remote Sens.* **2022**, *14*, 2628. [CrossRef]
150. Roy, D.P.; Huang, H.; Houborg, R.; Martins, V.S. A Global Analysis of the Temporal Availability of PlanetScope High Spatial Resolution Multi-Spectral Imagery. *Remote Sens. Environ.* **2021**, *264*, 112586. [CrossRef]
151. Collison, A.; Jumpasut, A.; Bourne, H. *On-Orbit Radiometric Calibration of the Planet Satellite Fleet Doves and Skysats*; USGS: Washington, DC, USA, 2022.
152. Mansaray, A.S.; Dzialowski, A.R.; Martin, M.E.; Wagner, K.L.; Gholizadeh, H.; Stoodley, S.H. Comparing PlanetScope to Landsat-8 and Sentinel-2 for Sensing Water Quality in Reservoirs in Agricultural Watersheds. *Remote Sens.* **2021**, *13*, 1847. [CrossRef]
153. Wang, H.; Gong, F.Y. Quantifying City- and Street-Scale Urban Tree Phenology from Landsat-8, Sentinel-2, and PlanetScope Images: A Case Study in Downtown Beijing. *Remote Sens.* **2024**, *16*, 2351. [CrossRef]

154. Latte, N.; Lejeune, P. PlanetScope Radiometric Normalization and Sentinel-2 Super-Resolution (2.5 m): A Straightforward Spectral-Spatial Fusion of Multi-Satellite Multi-Sensor Images Using Residual Convolutional Neural Networks. *Remote Sens.* **2020**, *12*, 2366. [CrossRef]
155. Ibrahim, S.; Balzter, H. Evaluating Flood Damage to Paddy Rice Fields Using PlanetScope and Sentinel-1 Data in North-Western Nigeria: Towards Potential Climate Adaptation Strategies. *Remote Sens.* **2024**, *16*, 3657. [CrossRef]
156. Digital Number Definition—ESRI GIS Dictionary. Available online: https://support.esri.com/en-us/gis-dictionary/digital-number (accessed on 6 October 2024).
157. Burt, J.E.; Barber, G.M.; Rigby, D.L. *Elementary Statistics for Geographers*, 3rd ed.; Guilford Press: Guilford, CO, USA, 2009.
158. Gonzalez, R.C.; Woods, R.E. *Digital Image Processing*; Pearson: London, UK, 2017.
159. John, A.R.; Jia, X. *Remote Sensing Digital Image Analysis*, 4th ed.; Springer: Berlin/Heidelberg, Germany, 2006.
160. Schowengerdt, R.A. *Remote Sensing: Models and Methods for Image Processing*, 3rd ed.; Elsevier: Amsterdam, The Netherlands, 2006.
161. Doelling, D.; Helder, D.; Schott, J.; Stone, T.; Pinto, C.T. 1.17—Vicarious Calibration and Validation. In *Comprehensive Remote Sensing*; Liang, S., Ed.; Elsevier: Oxford, UK, 2018; pp. 475–518, ISBN 978-0-12-803221-3.
162. Gascon, F.; Bouzinac, C.; Thépaut, O.; Jung, M.; Francesconi, B.; Louis, J.; Lonjou, V.; Lafrance, B.; Massera, S.; Gaudel-Vacaresse, A.; et al. Copernicus Sentinel-2A Calibration and Products Validation Status. *Remote Sens.* **2017**, *9*, 584. [CrossRef]
163. Szantoi, Z.; Strobl, P. Copernicus Sentinel-2 Calibration and Validation. *Eur. J. Remote Sens.* **2019**, *52*, 253–255. [CrossRef]
164. Blanchet, G.; Lebeque, L.; Fourest, S.; Latry, C.; Porez-Nadal, F.; Lacherade, S.; Thiebaut, C. Pleiades-hr innovative techniques for radiometric image quality commissioning. *Int. Arch. Photogramm. Remote Sens. Spat. Inf. Sci.* **2012**, *XXXIX-B1*, 513–518. [CrossRef]
165. Khadka, N.; Teixeira Pinto, C.; Leigh, L. Detection of Change Points in Pseudo-Invariant Calibration Sites Time Series Using Multi-Sensor Satellite Imagery. *Remote Sens.* **2021**, *13*, 2079. [CrossRef]
166. Varlyguin, D.; Roth, L.; Hulina, S.; Rayner, M.; Vrabel, J.; Avila, F.; Bresnahan, P.; Henry, L. Assessment of the Radiometric Calibration of PlanetScope 2 Dove Imagery. Available online: https://earth.esa.int/eogateway/documents/20142/1305226/JACIE-2017-DVarlyguin-GDA-NGA-ASMTofRadCal-PlanetScope2.pdf (accessed on 13 September 2024).
167. Li, S.; Ganguly, S.; Dungan, J.L.; Wang, W.; Nemani, R.R.; Li, S.; Ganguly, S.; Dungan, J.L.; Wang, W.; Nemani, R.R. Sentinel-2 MSI Radiometric Characterization and Cross-Calibration with Landsat-8 OLI. *Adv. Remote Sens.* **2017**, *6*, 147–159. [CrossRef]
168. Planet–Scene Level Normalization and Harmonization of Planet Dove Imagery. Available online: https://assets.planet.com/docs/scene_level_normalization_of_planet_dove_imagery.pdf (accessed on 1 February 2024).
169. Planet Imagery Product Specifications. Available online: https://earth.esa.int/eogateway/documents/20142/37627/Planet-combined-imagery-product-specs-2020.pdf (accessed on 31 July 2024).
170. Kington, J.; Collison, A. *Scene Level Normalization and Harmonization of Planet Dove Imagery*; Planet Labs Inc.: San Francisco, CA, USA, 2022.
171. Do You Provide Relative Spectral Response Curves (RSRs) for Your Satellites?—Welcome to Planet Support. Available online: https://support.planet.com/hc/en-us/articles/360014290293-Do-you-provide-Relative-Spectral-Response-Curves-RSRs-for-your-satellites (accessed on 31 July 2024).
172. Linear Regression—MATLAB & Simulink—MathWorks Italia. Available online: https://it.mathworks.com/help/matlab/data_analysis/linear-regression.html (accessed on 31 July 2024).
173. Fit Linear Regression Model—MATLAB Fitlm—MathWorks Italia. Available online: https://it.mathworks.com/help/stats/fitlm.html (accessed on 31 July 2024).
174. Wegener, M. Destriping Multiple Sensor Imagery by Improved Histogram Matching. *Int. J. Remote Sens.* **1990**, *11*, 859–875. [CrossRef]
175. Histogram Matching. How to Generate a Histogram for An. . . | by Ali Pourramezan Fard | Towards Data Science. Available online: https://towardsdatascience.com/histogram-matching-ee3a67b4cbc1 (accessed on 31 July 2024).
176. Adjust Histogram of 2-D Image to Match Histogram of Reference Image—MATLAB Imhistmatch—MathWorks Italia. Available online: https://it.mathworks.com/help/images/ref/imhistmatch.html (accessed on 31 July 2024).
177. Abdel-Nabi, H.; Al-Haj, A. Frequency Domain Based Data Hiding for Encrypted Medical Images. In *Intelligent Data Security Solutions for e-Health Applications*; Academic Press: Cambridge, MA, USA, 2020; pp. 21–56. [CrossRef]
178. Chavez Jr, P. Image-Based Atmospheric Corrections—Revisited and Improved. *Photogramm. Eng. Remote Sens.* **1996**, *62*, 1025–1036.
179. Song, C.; Woodcock, C.E.; Seto, K.C.; Lenney, M.P.; Macomber, S.A. Classification and Change Detection Using Landsat TM Data: When and How to Correct Atmospheric Effects? *Remote Sens. Environ.* **2001**, *75*, 230–244. [CrossRef]
180. Vermote, E.F.; Tanre, D.; Deuze, J.L.; Herman, M.; Morcette, J.-J. Second Simulation of the Satellite Signal in the Solar Spectrum, 6S: An Overview. *IEEE Trans. Geosci. Remote Sens.* **1997**, *35*, 675–686. [CrossRef]
181. The Riserva San Massimo ⋆ Riserva San Massimo. Available online: https://riservasanmassimo.net/?lang=en (accessed on 31 July 2024).
182. Martina Di Iorio Il riso Migliore d'Italia Cresce in una Riserva Naturale a due Passi da Milano. Available online: https://www.milanotoday.it/cibo/riserva-san-massimo-storia-del-riso-migliore-d-italia.html (accessed on 6 October 2024).
183. Ezio Zigliani Gambero Rosso: Il Miglior Riso Carnaroli è Riserva San Massimo. Available online: https://corrieredelvino.it/news/gambero-rosso-il-miglior-riso-carnaroli-e-riserva-san-massimo/ (accessed on 6 October 2024).
184. Giovanni Chiodini Riserva San Massimo, Dal Ticino Un Riso per Sceicchi. Available online: https://www.ilgiorno.it/cronaca/ticino-riso-carnaroli-d48bd91f (accessed on 6 October 2024).

185. Mara Nocilla Salvano Il Prezioso Riso Carnaroli Dal Cambiamento Climatico Utilizzando Una Tecnica Innovativa. Available online: https://www.gamberorosso.it/notizie/riso-carnaroli-riserva-san-massimo/ (accessed on 6 October 2024).
186. Riso Carnaroli Riserva San Massimo Protagonista Della Sfida in Esterna. Available online: https://masterchef.sky.it/foto/riso-carnaroli-riserva-san-massimo-protagonista-della-sfida-in-esterna#00 (accessed on 6 October 2024).
187. Sentinel-2 User Handbook. Available online: https://sentinel.esa.int/documents/247904/685211/Sentinel-2_User_Handbook (accessed on 1 February 2024).
188. Copernicus. Available online: https://www.esa.int/Applications/Observing_the_Earth/Copernicus (accessed on 1 February 2024).
189. Sentinel-2 The Mission. Available online: https://www.esa.int/Applications/Observing_the_Earth/Copernicus/Sentinel-2 (accessed on 1 February 2024).
190. Sentinel-2 MSI Technical Guide. Available online: https://sentinel.esa.int/web/sentinel/technical-guides/sentinel-2-msi (accessed on 1 February 2024).
191. About Copernicus. Available online: https://www.copernicus.eu/en/about-copernicus (accessed on 1 February 2024).
192. Sentinel-2A (10 m) Satellite Sensor–Satellite Imaging Corporation. Available online: https://www.satimagingcorp.com/satellite-sensors/other-satellite-sensors/sentinel-2a/ (accessed on 1 February 2024).
193. Sentinel-2 MSI User Guide. Available online: https://sentinel.esa.int/web/sentinel/user-guides/sentinel-2-msi (accessed on 1 February 2024).
194. Sentinel-2 License. Available online: https://open.esa.int/copernicus-sentinel-satellite-imagery-under-open-licence/ (accessed on 1 February 2024).
195. PlanetScope. Available online: https://developers.planet.com/docs/data/planetscope/ (accessed on 31 July 2024).
196. Understanding PlanetScope Instruments. Available online: https://developers.planet.com/docs/apis/data/sensors/ (accessed on 1 February 2024).
197. Planet Imagery Product Specifications. Available online: https://assets.planet.com/docs/Planet_Combined_Imagery_Product_Specs_letter_screen.pdf (accessed on 1 February 2024).
198. Planet—PSScene. Available online: https://developers.planet.com/docs/data/psscene/ (accessed on 1 February 2024).
199. Licensing Information Center | Planet. Available online: https://www.planet.com/licensing-information/ (accessed on 31 July 2024).
200. Planetscope Harmonized Bands with Sentinel-2, Community Overview. Available online: https://community.planet.com/planetscope-76/planetscope-harmonized-bands-with-sentinel-2-469 (accessed on 18 October 2024).
201. Curdoglo, M. Reprocessing SuperDove/Dove-R Archive with Band Alignment Improvements External Content. Available online: https://support.planet.com/hc/en-us/articles/7545698265117-Reprocessing-Superdove-Dove-R-Archive-With-Band-Alignment-Improvements (accessed on 18 October 2024).
202. Zhang, H.K.; Roy, D.P.; Yan, L.; Li, Z.; Huang, H.; Vermote, E.; Skakun, S.; Roger, J.C. Characterization of Sentinel-2A and Landsat-8 Top of Atmosphere, Surface, and Nadir BRDF Adjusted Reflectance and NDVI Differences. *Remote Sens. Environ.* **2018**, *215*, 482–494. [CrossRef]
203. SkySat. Available online: https://developers.planet.com/docs/data/skysat/ (accessed on 31 July 2024).
204. Skysat Imagery Product Specification. Available online: https://assets.planet.com/marketing/PDF/SkySat-Ortho-Scene-Product-Spec-Sheet.pdf (accessed on 31 July 2024).
205. Combine (Spatial Analyst)—ArcGIS Pro | Documentation. Available online: https://pro.arcgis.com/en/pro-app/latest/tool-reference/spatial-analyst/combine.htm (accessed on 31 July 2024).
206. Liedtke, J.; Hu, H. ArcGIS Pro: Image Segmentation, Classification, and Machine Learning. Available online: https://proceedings.esri.com/library/userconf/proc18/tech-workshops/tw_1666-182.pdf (accessed on 31 July 2024).
207. Parashar, N. Classification Techniques in Remote Sensing: A Review. *Commun. Comput. Inf. Sci.* **2023**, *1893*, 40–50. [CrossRef]
208. ur Rehman, A.; Belhaouari, S.B. Unsupervised Outlier Detection in Multidimensional Data. *J. Big Data* **2021**, *8*, 80. [CrossRef]
209. ROI-Based Processing—MATLAB & Simulink—MathWorks Italia. Available online: https://it.mathworks.com/help/images/roi-based-processing.html (accessed on 31 July 2024).
210. Studley, H. *Comparison of Image Resampling Techniques for Satellite Imagery*; Semantic Scholar: Seattle, WA, USA, 2011. Available online: https://www.semanticscholar.org/paper/Comparison-of-Image-Resampling-Techniques-for-Studley/fa316fc18b22fe466f818bcea0edae76d08c91f9 (accessed on 31 July 2024).
211. Lyons, M.B.; Keith, D.A.; Phinn, S.R.; Mason, T.J.; Elith, J. A Comparison of Resampling Methods for Remote Sensing Classification and Accuracy Assessment. *Remote Sens. Environ.* **2018**, *208*, 145–153. [CrossRef]
212. Resample (Data Management)—ArcGIS Pro | Documentation. Available online: https://pro.arcgis.com/en/pro-app/latest/tool-reference/data-management/resample.htm (accessed on 31 July 2024).
213. Cell Size and Resampling in Analysis—ArcGIS Pro | Documentation. Available online: https://pro.arcgis.com/en/pro-app/latest/help/analysis/spatial-analyst/performing-analysis/cell-size-and-resampling-in-analysis.htm (accessed on 31 July 2024).
214. Mathworks Interpret Linear Regression Results—Matlab. Available online: https://it.mathworks.com/help/stats/understanding-linear-regression-outputs.html (accessed on 9 October 2024).
215. Wang, J.; Ou, B. Video Reversible Data Hiding: A Systematic Review. *J. Vis. Commun. Image Represent.* **2024**, *98*, 104029. [CrossRef]

216. Mehran, Z.Y.; Nafari, M.; Nafari, A.; Zandi Mehran, N. Histogram Shifting as a Data Hiding Technique: An Overview of Recent Developments. *Commun. Comput. Inf. Sci.* **2011**, *166*, 770–786. [CrossRef]
217. 14.2-Cumulative Distribution Functions | STAT 414. Available online: https://online.stat.psu.edu/stat414/lesson/14/14.2 (accessed on 31 July 2024).
218. Pontius, R.G.; Thontteh, O.; Chen, H. Components of Information for Multiple Resolution Comparison between Maps That Share a Real Variable. *Environ. Ecol. Stat.* **2008**, *15*, 111–142. [CrossRef]

Disclaimer/Publisher's Note: The statements, opinions and data contained in all publications are solely those of the individual author(s) and contributor(s) and not of MDPI and/or the editor(s). MDPI and/or the editor(s) disclaim responsibility for any injury to people or property resulting from any ideas, methods, instructions or products referred to in the content.